White Rose Research Online

eprints@whiterose.ac.uk
https://eprints.whiterose.ac.uk
Universities of Leeds, Sheffield and York

Deposited via The University of Leeds.

White Rose Research Online URL for this paper:
https://eprints.whiterose.ac.uk/id/eprint/90126/

Version: Accepted Version

Article:
He, Y-X, Angus, DA, Yuan, SY et al. (2015) Feasibility of time-lapse AVO and AVOA analysis to monitor compaction-induced seismic anisotropy. Journal of Applied Geophysics, 122. 134 - 148. ISSN: 0926-9851

https://doi.org/10.1016/j.jappgeo.2015.09.010

© 2015, Elsevier. Licensed under the Creative Commons Attribution-NonCommercial-NoDerivatives 4.0 International http://creativecommons.org/licenses/by-nc-nd/4.0/

Reuse
Items deposited in White Rose Research Online are protected by copyright, with all rights reserved unless indicated otherwise. They may be downloaded and/or printed for private study, or other acts as permitted by national copyright laws. The publisher or other rights holders may allow further reproduction and re-use of the full text version. This is indicated by the licence information on the White Rose Research Online record for the item.

Takedown
If you consider content in White Rose Research Online to be in breach of UK law, please notify us by emailing eprints@whiterose.ac.uk including the URL of the record and the reason for the withdrawal request.

UNIVERSITY OF LEEDS
University of Sheffield
UNIVERSITY of York

Feasibility of time-lapse AVO and AVOA analysis to monitor compaction-induced seismic anisotropy

Y.-X. He[1]*, D.A. Angus[1], S.Y. Yuan[2] and Y.G. Xu[3]

[1]School of Earth and Environment, University of Leeds, Leeds, LS2 9JT, United Kingdom.

[2]College of Geophysics and Information Engineering, China University of Petroleum-Beijing, Beijing, China.

[3]Department of Earth Science and Engineering, Imperial College London, London, United Kingdom.

*Corresponding author E-mail: *eeyhe123@gmail.com,* Tel*: +86 15811485456*

Abstract

Hydrocarbon reservoir production generally results in observable time-lapse physical properties changes, such as velocity increases within a compacting reservoir. However, the physical property changes that lead to velocity changes can be difficult to isolate uniquely. Thus, integrated hydro-mechanical simulation, stress-sensitive rock physics models and time-lapse seismic modelling workflows can be employed to study the influence of velocity changes and induced seismic anisotropy due to reservoir compaction. We study the influence of reservoir compaction and compartmentalization on time-lapse seismic signatures for reflection amplitude variation with offset (AVO) and azimuth (AVOA). Specifically, the time-lapse AVO and AVOA responses are predicted for two models: a laterally homogeneous four-layer dipping model and a laterally heterogeneous graben structure reservoir model. Seismic reflection coefficients for different offsets and azimuths are calculated for compressional (P-P) and converted shear (P-S) waves using an anisotropic ray tracer as well as using approximate equations for AVO and AVOA. The simulations help assess the feasibility of using time-lapse AVO and AVOA signatures to monitor reservoir compartmentalization as well as evaluate induced stress anisotropy due to changes in the effective stress field. The results of this study indicate that time-lapse AVO and AVOA analysis can be applied as a potential means for qualitatively and semi-quantitatively linking azimuthal anisotropy changes caused by reservoir production to pressure/stress changes.

Keywords: Time-lapse Seismic Analysis, Reservoir Compaction, Hydro-mechanical Simulation, Seismic Anisotropy, Azimuthal AVO

1. Introduction

Most crustal rocks are seismically anisotropic and as such seismic data can display various kinds of azimuthal anisotropic patterns and anisotropic strength (e.g., Liu and Martinez 2012). The strength or magnitude of seismic anisotropy typically ranges between 2%-6% (e.g., Jenner and Williams 2003; Zheng 2006; Liu and Martinez 2012) and thus may contribute to difficulties in conventional seismic processing, imaging and interpretation. Recently, it has been recognised that reservoir production can induce seismic anisotropy within and surrounding the producing reservoir due to deformation and changes in the stress field (e.g., Olofsson et al. 2003; Herwanger and Horne 2009). Thus measuring time-lapse seismic anisotropy can be used to monitor the state of stress and strain within a producing reservoir system, with potential to assess reservoir compartmentalization and reduce geomechanical risk (e.g., He et al. 2015a; He et al. 2015b, in press).

The time-lapse seismic method is capable of monitoring changes in subsurface physical properties, and can be grouped into two classes: travel-time methods and reflection amplitude methods (e.g., Calvert 2005; Dimri et al. 2012; Johnson 2013; Wang et al. 2010). Time-lapse seismic travel-time shifts embody the path-averaged combined influence of velocity changes and strains. Time-lapse seismic reflection amplitude changes are sensitive to perturbations in localised properties, such as velocity and density changes across a boundary. Changes in reflectivity along the top and bottom of reservoir horizons are mainly due to a combination of changes in pore pressure, fluid saturation and rock deformation. For instance, the time-lapse seismic reflection amplitude variation with offset (AVO) method has been applied with various degrees of success to discriminate between changes in reservoir pressure and fluid saturation (e.g., Landrø 2001; Stovas and Landrø 2005; Herwanger and Koutsabeloulis 2011). However, hydrocarbon depletion induced reservoir compaction and stress arching can cause seismic anisotropy and hence distort the AVO response for wide-azimuth and long-offset data (e.g., Herwanger and Horne 2009). Thus consideration of anisotropy effects on the reflectivity response of a producing reservoir should be also incorporated.

The seismic P-wave amplitude variation with offset and azimuth (AVOA) technique was developed for detecting sub-seismic vertical fracture sets. These vertical to sub-vertical fracture sets manifest in

the form of observable horizontal transverse isotropy (HTI) medium (e.g., Liu and Martinez 2012). HTI is the simplest form of azimuthal anisotropy, and has been observed in both carbonate and sandstone reservoirs (e.g., Rüger 1997, 1998; Jenner 2002; Hall and Kendall 2003; Olofsson et al. 2003; Duxbury et al. 2012). Thus, in principal, detecting time-lapse changes in seismic azimuthal anisotropy during hydrocarbon production using the AVOA technique might be feasible for monitoring subtle subsurface changes in the stress field. Such changes in the stress field could be used to identify reservoir compartmentalization, and hence allow for better dynamic reservoir characterization (e.g., Hall and MacBeth 2001; Shams and MacBeth 2003; Al-Naamani et al. 2004; Mattocks et al. 2005; MacBeth and Shams 2006). However, subsurface structure, such as dipping horizons in an isotropic medium, can generate 'false' azimuthal variations of amplitude reflectivity similar to that introduced by seismic azimuthal anisotropy (e.g., Jenner and Williams 2003; Zheng 2006). Thus, the influence of subsurface geometry must be accounted for prior to applying AVOA technique to interpret time-lapse seismic observations.

In this study, the influence of reservoir production induced seismic anisotropy and velocity heterogeneity on time-lapse AVO and AVOA responses is investigated. To do this, the effect of inherent (or background) anisotropy and induced (or dynamic) anisotropy (i.e., seismic anisotropy induced during reservoir depletion) on time-lapse seismic analysis is studied. The primary aim of this research is to explore the potential of applying AVO and AVOA analysis as a time-lapse seismic reservoir monitoring tool for geomechanical risk assessment and model calibration. Time-lapse seismic P-P wave (incident P-wave reflected as P-wave) and P-S wave (incident P-wave reflected as converted S-wave) AVO and AVOA analysis is implemented for wide-azimuth, long-offset data for two synthetic models: a simple four-layer reservoir model with a dipping horizon and a hydro-mechanical graben-style reservoir model having three compartments offset by two normal faults (see Angus et al., 2010 for description of the hydro-mechanical model). The simple four-layer model is used to test the influence of existing dip and production induced velocity anisotropy on the seismic azimuthal response of the reflection coefficient for both P-P and P-S waves. The hydro-mechanical two-fault model represents a more realistic scenario being applied to explore the influence of induced velocity heterogeneity as well as induced seismic anisotropy on the time-lapse seismic reflection amplitude response.

2. Theoretical background

To correctly model the seismic response due to 1-D structure one needs to consider the interaction of the incident elastic wave with a discontinuity in material properties. The energy of the primary wave can be converted into up to six secondary waves. Although Snell's law can be used to determine the directional properties of all the secondary waves, it cannot provide information on waveform amplitudes and pulse distortion (e.g., Yuan et al. 2014). Thus a more complete evaluation of the reflection and transmission (R/T) properties is needed. Over the past several decades significant contributions have been made in the evaluation of R/T coefficients for isotropic (e.g., Gilbert and Backus 1966; Molotkov et al. 1976; Kennett 1983) and anisotropic (e.g., Garmany 1983; Fryer and Frazer 1984; Guest et al. 1993) layered media. In most of these approaches, the solution to the R/T response involves using a local plane-wave and plane-boundary approximation (see Hudson 1980; Kennett1983), and thereby Guest and Kendall (1993) implement an anisotropic extension of the layer matrix R/T coefficients (see Angus and Thomson 2012). For instance, an anisotropic ray tracer ATRAK (Guest and Kendall 1993) is based on asymptotic ray theory and Hamiltonian solution, and allows studying travel-time effects in smoothly varying heterogeneous and anisotropic media as well as some amplitude effects and waveform distortions. These exact solutions for anisotropic media, although elegant, may not be computationally tractable compared to approximate solutions. In this section, we summarise the various approximate approaches developed from the Zoeppritz Equations to calculate the reflection coefficients for AVO and AVOA analysis. For more details on the exact solution of the reflection coefficient for plane interfaces the reader is referred to Kennett (1983) and Angus and Thomson (2012).

For isotropic media, the approximate solution for the P-P wave reflection coefficient as a function of incidence phase angle (θ) is written as (Rüger 1997)

$$R_P(\theta) = \frac{1}{2}\frac{\Delta Z}{\overline{Z}} + \frac{1}{2}\left\{\frac{\Delta\alpha}{\overline{\alpha}} - \left(\frac{2\overline{\beta}}{\overline{\alpha}}\right)^2 \frac{\Delta G}{\overline{G}}\right\}\sin^2\theta + \frac{1}{2}\frac{\Delta\alpha}{\overline{\alpha}}\sin^2\theta\tan^2\theta, \quad (1)$$

where $\alpha = \sqrt{c_{33}/\rho}$ and $\beta = \sqrt{c_{44}/\rho}$ are the vertical P- and S-wave velocities respectively, the upper "bar" term represents the averaged value of the lower and upper medium elastic parameters, Δ represents the physical property contrast across the reflecting boundary, $Z = \rho\alpha$ is the normal-

incidence P-wave impedance, and $G = \rho\beta^2$ is the shear modulus for normal-incidence S-wave. Equation (1) is valid for small discontinuities in elastic properties across the interface and is restricted to incidence angles of up to 30°. Equation (1) has been used to compute the AVO response in various studies (e.g., Rüger 1997; Landrø 2001; Jing et al. 2006).

AVO analysis has been applied also to converted (P-S) waves because they can provide useful additional information to that of conventional P-P wave AVO. For instance, converted shear waves are affected less during propagation through overburden gas clouds than compressional waves (e.g., Jing et al. 2006) and they also provide higher resolution. For isotropic media, Ramos and Castagna (2001) approximate the P-S wave reflection coefficient as a function of incidence phase angle as

$$R_{PS}(\theta) \approx A_1 \sin\theta + B_1 \sin^3\theta + C_1 \sin^5\theta, \tag{2a}$$

where

$$A_1 = \left[-2\frac{\overline{\beta}}{\overline{\alpha}}\frac{\Delta\beta}{\overline{\beta}}\right] - \left[\left(\frac{1}{2} + \frac{\overline{\beta}}{\overline{\alpha}}\right)\frac{\Delta\rho}{\overline{\rho}}\right], \tag{2b}$$

$$B_1 = \left[\left(\frac{2\overline{\beta}^2}{\overline{\alpha}^2} + \frac{\overline{\beta}}{\overline{\alpha}}\right)\frac{\Delta\beta}{\overline{\beta}}\right] + \left[\left(\frac{3}{4}\frac{\overline{\beta}^2}{\overline{\alpha}^2} + \frac{\overline{\beta}}{2\overline{\alpha}}\right)\frac{\Delta\rho}{\overline{\rho}}\right], \tag{2c}$$

$$C_1 = \left[\left(\frac{\overline{\beta}}{\overline{\alpha}}\right)^4 \frac{\Delta\beta}{\overline{\beta}}\right] + \left[\frac{1}{2}\left(\frac{\overline{\beta}}{\overline{\alpha}}\right)^4 \frac{\Delta\rho}{\overline{\rho}}\right]. \tag{2d}$$

Equation (2) is valid for small elastic contrasts and is restricted to incidence angles of typically less than 30°.

For an interface between two vertical transverse isotropic (VTI) half-spaces, Rüger (1997) approximates the P-P wave reflectivity variation with incidence angle using the linearized equation

$$R_P^{VTI}(\theta) = \frac{1}{2}\frac{\Delta Z}{\overline{Z}} + \frac{1}{2}\left\{\frac{\Delta\alpha}{\overline{\alpha}} - \left(\frac{2\overline{\beta}}{\overline{\alpha}}\right)^2 \frac{\Delta G}{\overline{G}} + \Delta\delta\right\}\sin^2\theta + \frac{1}{2}\left\{\frac{\Delta\alpha}{\overline{\alpha}} + \Delta\varepsilon\right\}\sin^2\theta\tan^2\theta, \tag{3}$$

where ε and δ are Thomsen's parameters for weakly anisotropic VTI media (Thomsen 1986). Equation (3) is valid for small elastic contrasts and reduces to the isotropic AVO equation (1) when

the Thomsen anisotropy parameters ε and δ are both zero. For VTI media, there is no azimuthal dependence and so equation (3) is only a function of incidence angle (offset).

For HTI media, the seismic wave velocity varies with azimuth and so HTI media is often referred to as azimuthally anisotropic media. Therefore, for HTI media the reflection amplitude varies with incidence angle as well as azimuthal angle. It has been recognised that due to the presence of fractures and joints most crustal rocks down to 10 km to 20 km display features of effective azimuthal anisotropy (e.g., Crampin 1985). For an interface between two HTI half-spaces with the same symmetry axis orientation but not necessarily same anisotropic strength, Rüger (1997, 1998) extends equation (3) to approximate the P-P wave reflectivity. The approximate reflection coefficient for a compressional plane wave in HTI media as a function of incidence angle (θ) and azimuthal angle (ϕ) is given by Rüger (1998) as

$$R_p^{HTI}(\theta,\phi) = \frac{1}{2}\frac{\Delta Z}{\overline{Z}} + \frac{1}{2}\left\{\frac{\Delta\alpha}{\overline{\alpha}} - \left(\frac{2\overline{\beta}}{\overline{\alpha}}\right)^2\frac{\Delta G}{\overline{G}} + \left[\Delta\delta^{(V)} + 2\left(\frac{2\overline{\beta}}{\overline{\alpha}}\right)^2\Delta\gamma\right]\cos^2\phi\right\}\sin^2\theta + \frac{1}{2}\left\{\frac{\Delta\alpha}{\overline{\alpha}} + \Delta\varepsilon^{(V)}\cos^2\phi + \Delta\delta^{(V)}\sin^2\phi\cos^2\phi\right\}\sin^2\theta\tan^2\theta, \quad (4a)$$

where ϕ represents the azimuthal phase angle defined with respect to the symmetry axis and γ is the third Thomsen anisotropy parameter (Thomsen 1986). The effective Thomsen anisotropy parameters $\varepsilon^{(V)}$ and $\delta^{(V)}$ for HTI medium are defined as (e.g., Rüger 1997; Tsvankin 1997)

$$\varepsilon^{(V)} = -\frac{\varepsilon}{1+2\varepsilon}, \quad (4b)$$

$$\delta^{(V)} = \frac{\delta - 2\varepsilon\left[1+(\varepsilon/f)\right]}{(1+2\varepsilon)\left[1+(2\varepsilon/f)\right]}, \quad (4c)$$

$$f = 1-(\alpha/\beta)^2. \quad (4d)$$

For small incidence angles (typically ≤30°), the higher order $\sin^2\theta\tan^2\theta$ term can be ignored and the behaviour of $R_p^{HTI}(\theta,\phi)$ can be simplified by using the AVOA intercept (P-wave normal-incidence reflectivity A) and two gradients: an azimuthally invariant isotropic component G_{iso} and an azimuthally dependent anisotropic contribution G_{aniso} (see Rüger 1998; Jenner 2002)

$$R_P^{HTI}(\theta,\phi) = A + \left(G_{iso} + G_{aniso}\cos^2\phi\right)\sin^2\theta, \tag{5a}$$

where

$$A = \frac{1}{2}\frac{\Delta Z}{\overline{Z}}, \tag{5b}$$

$$G_{iso} = \frac{1}{2}\left[\frac{\Delta\alpha}{\overline{\alpha}} - \left(\frac{2\overline{\beta}}{\overline{\alpha}}\right)^2 \frac{\Delta G}{\overline{G}}\right], \tag{5c}$$

$$G_{aniso} = \frac{1}{2}\left[\Delta\delta^{(V)} + 2\left(\frac{2\overline{\beta}}{\overline{\alpha}}\right)^2 \Delta\gamma\right]. \tag{5d}$$

It should be noted that the magnitude of the gradient G_{aniso} is a function of the contrast in the anisotropy parameters $\delta^{(V)}$ and γ.

3. Results for two synthetic models

In this section, the results from numerical simulation from two models are discussed; a simple four-layer reservoir model having a dipping reflector, and a hydro-mechanical graben-structure reservoir model. We evaluate the approximate reflection amplitude coefficients to examine the feasibility of applying time-lapse seismic AVO and AVOA response to assess the effect of reservoir compaction induced triaxial stress changes and azimuthal velocity anisotropy. We seek to determine whether these attributes can be used to help identify reservoir compartmentalization.

3.1. Four-layer reservoir model

- **Methodology**

In Figure 1, a 2.5-D (invariantin the y-direction) four-layer elastic model is used to investigate the impact of dip (6^o with respect to the horizonal, x, axis) on time-lapse seismic reflection amplitude azimuthal measurements. Jenner and Williams (2003) note that dips on the order of 10^o can lead to an apparent velocity anisotropy of 4% and so a dip of 6^o should yield a comparable degree of anisotropy to that expected of production-induced anisotropy. For this dipping-layered reservoir model, the AVO and AVOA responses for both P-P and P-S waves are examined.

In this model, the third layer represents the producing reservoir that develops induced seismic anisotropy caused by changes in the effective stress field. The other layers within the model are static, and are homogeneous and isotropic. Three cases of induced anisotropy are examined within the reservoir and their values are based on sandstone measurements taken from the more realistic hydro-mechaical two-fault resevoir model of Angus et al. (2010). The three cases are all VTI and vary in terms of anisotropy strength: (i) weak anisotropy $\varepsilon = 0.026$, $\gamma = 0.018$ and $\delta = 0.007$ (anisotropy1); (ii) moderate anisotropy $\varepsilon = 0.046$, $\gamma = 0.057$ and $\delta = 0.007$ (anisotropy2); and (iii) strong anisotropy $\varepsilon = 0.105$, $\gamma = 0.102$ and $\delta = 0.006$ (anisotropy3). Figure 2 shows an example of rays traced in the dipping layer model using the anisotropic ray tracer ATRAK. For the selected horizon, ATRAK is used to calculate the reflection amplitude for each ray as a function of offset and azimuth for both the P-P and P-S waves. In this model, only the elastic properties within the reservoir change.

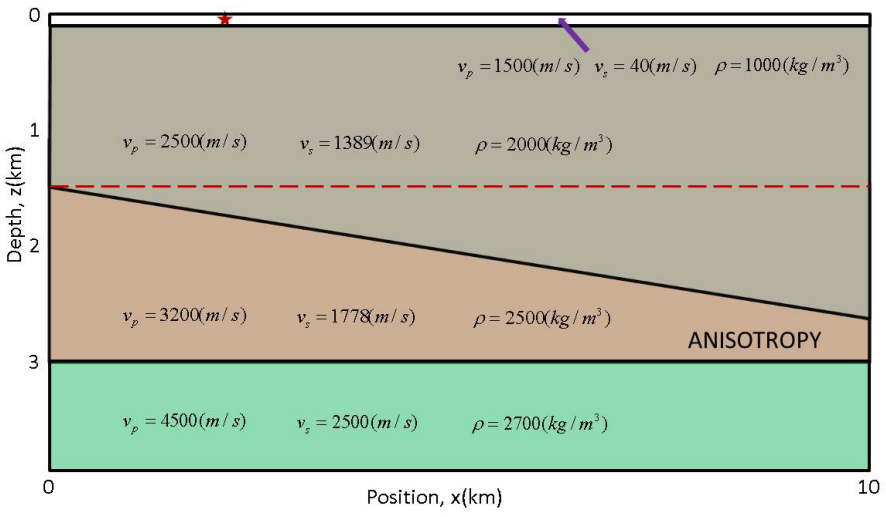

Figure 1. A 2.5-D synthetic four-layer earth model having a dipping reflector used in the ray tracing to compute the reflection amplitude variation with offset and azimuth. The third layer (i.e., reservoir unit) is modelled as initially isotropic that subsequently develops induced anisotropy due to reservoir production. The other layers are isotropic. The top layer represents the ocean (or water) layer (the arrow). The dashed red line represents a scenario where the top reservoir is horizontal flat, and the red star represents the source location. Velocities and bulk density are displayed within the figure.

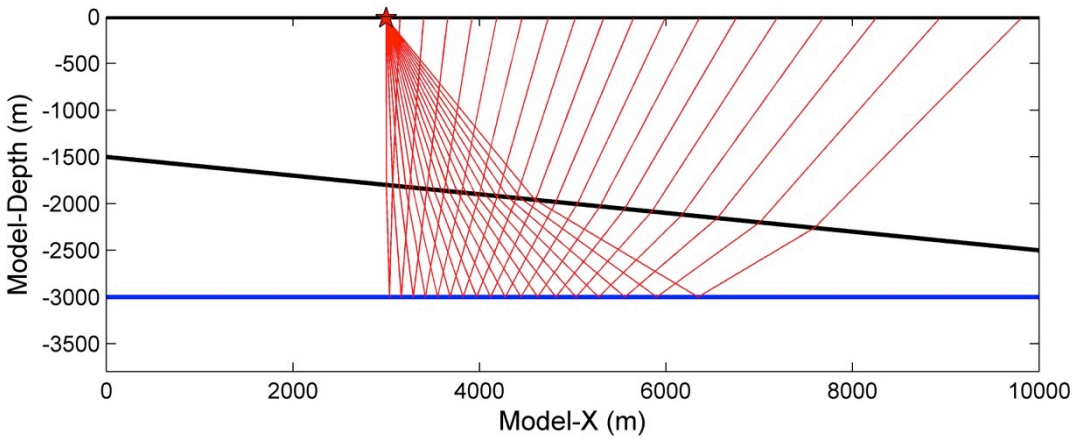

Figure 2. Rays traced through the four-layer elastic model (see Figure 1) from a source within the water layer at X=3000 m, and reflected off the bottom reservoir interface at 3000 m depth (blue line) for the P-P wave. The geophones are fixed along the bottom of the water layer.

■ Results

In Figure 3, the P-P wave and P-S_1wave (S_1 being the fast S-wave) reflection coefficients are shown for azimuth $\phi = 0^o$ (i.e., the shot-receiver gather is perpendicular to the strike ofthe dipping layer). As expected, the development of induced anisotropy within the layer from the background isotropy leads to noticeable changes in the P-P and P-S wave amplitudes. In Figures 4 and 5, the P-P and P-S_1 wave reflection coefficients for several azimuths ($\phi = 0^o, 30^o, 60^o$ and 90^o) are displayed for the background isotropic as well as the induced anisotropic models. It can be observed that for the VTI medium model, where there should be no azimuthal variation in elastic properties, the presence of dip influences the measurements for the different azimuths on the same order of magnitude as the induced anisotropy. This highlights the need to properly compensate for subsurface structure prior to time-lapse AVO and AVOA analysis.

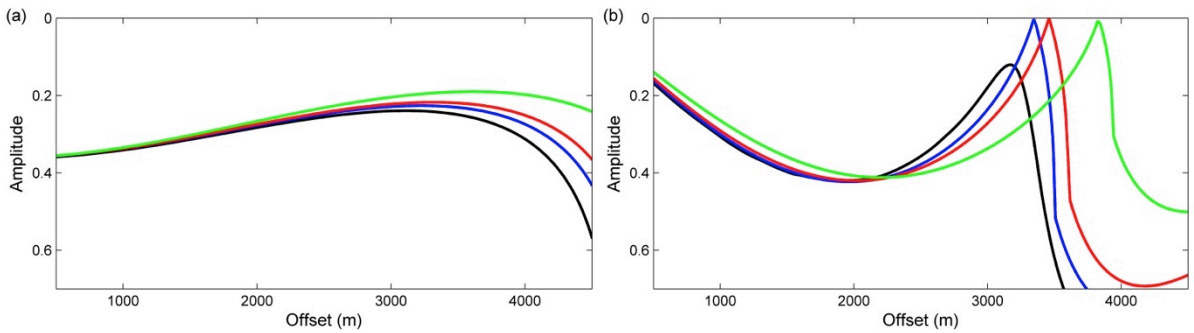

Figure 3. Seismic reflection coefficients for the (a) P-P and (b) P-S_1 waves are shown for the background isotropic and induced anisotropic models, using the ray tracer along the X-direction (i.e., azimuth of $\phi = 0^o$). The computed reflection coefficients are shown, with the black curve for the isotropic model, the blue curve for the weak anisotropic (anisotropy1) model, the red curve for the moderate anisotropic (anisotropy2) model and the green curve for the strong anisotropic (anisotropy3) model.

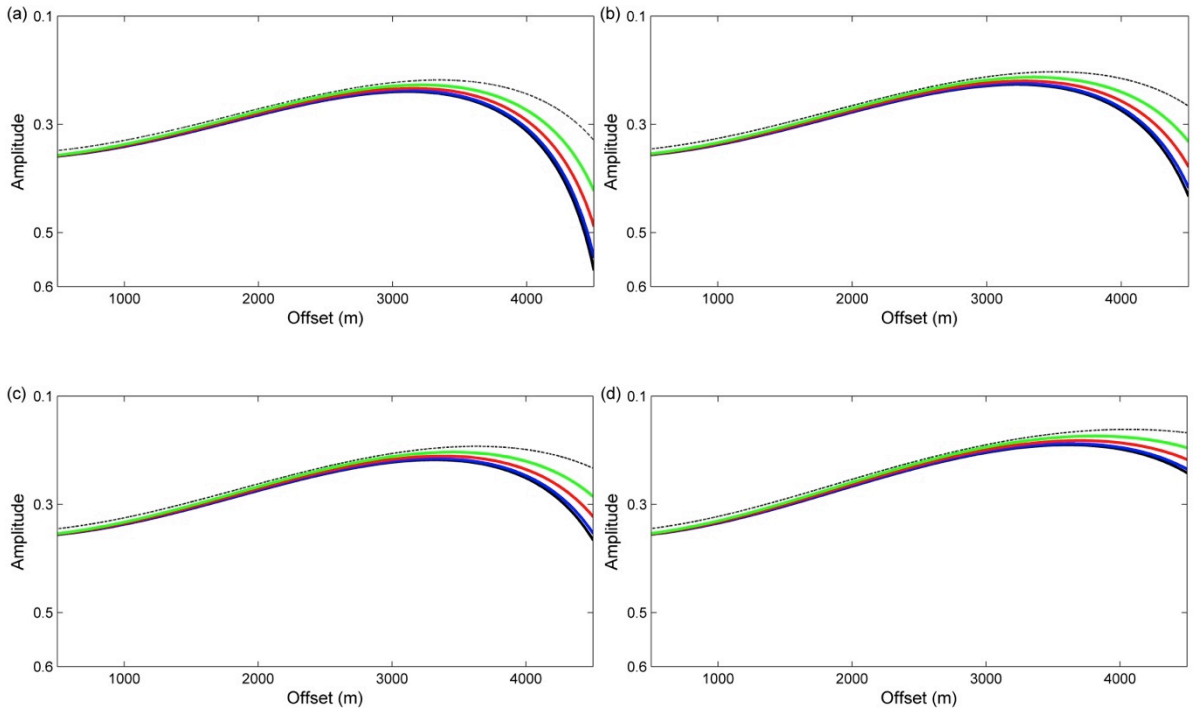

Figure 4. Seismic reflection coefficients for P-P waves are shown for the (a) isotropic, (b) weak anisotropic (anisotropy1), (c) moderate anisotropic (anisotropy2) and (d) strong anisotropic (anisotropy3) models, calculated using the ray tracer at four azimuths. The computed reflection coefficients are shown for azimuths: $\phi = 0^o$ (black curve), $\phi = 30^o$ (blue curve), $\phi = 60^o$ (red curve) and $\phi = 90^o$ (green curve). For comparison, the dotted-black curve represents the reflection amplitudes for the flat horizon model (shown by the dashed red line in Figure 1). Since the anisotropic models are VTI, there is no variation with azimuth for the flat horizon model.

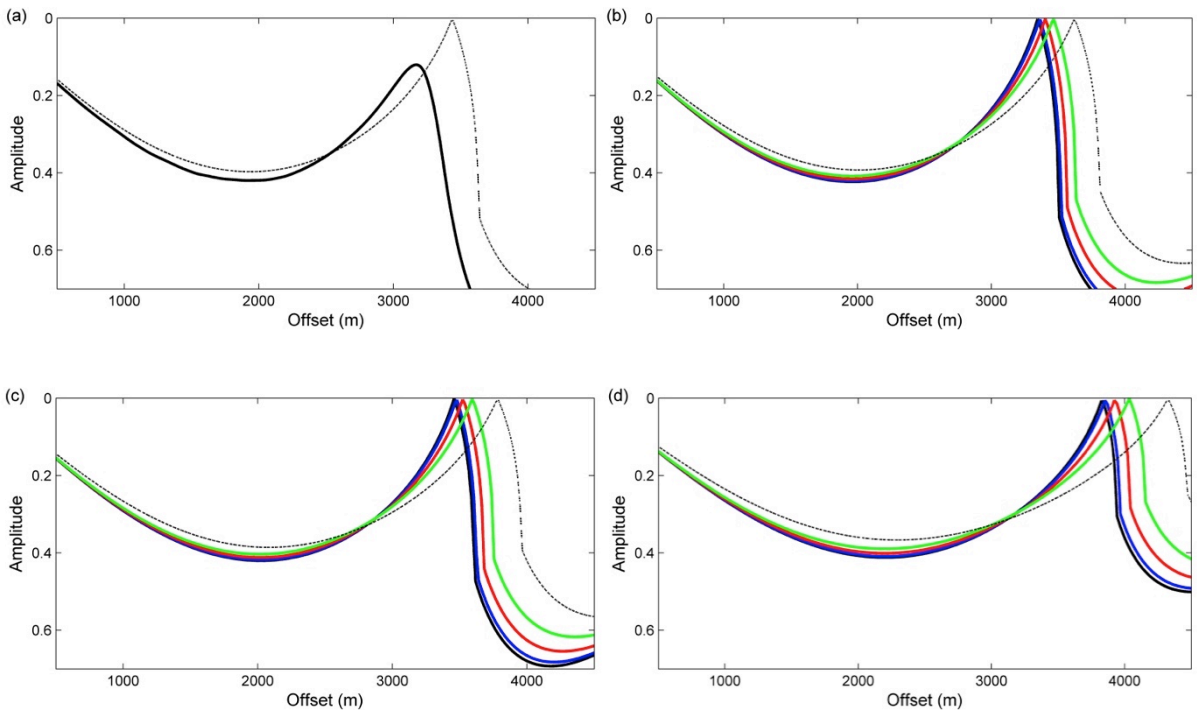

Figure 5. Seismic reflection coefficients for P-S_1 waves are shown for the (a) isotropic, (b) weak anisotropic (anisotropy1), (c) moderate anisotropic (anisotropy2) and (d) strong anisotropic (anisotropy3) models, calculated using the ray tracer at four azimuths. The computed reflection coefficients are shown for azimuths: $\phi = 0^o$ (black curve), $\phi = 30^o$ (blue curve), $\phi = 60^o$ (red curve) and $\phi = 90^o$ (green curve). For comparison, the dotted-black curve represents the reflection amplitudes for the flat horizon model (shown by the dashed red line in Figure 1). Since the anisotropic models are VTI, there is no variation with azimuth for the flat horizon model. P-S_1 waves reflection coefficients for the isotropic model at the other three azimuths (i.e., $\phi = 30^o$, 60^o and 90^o) are too small and thus not displayed.

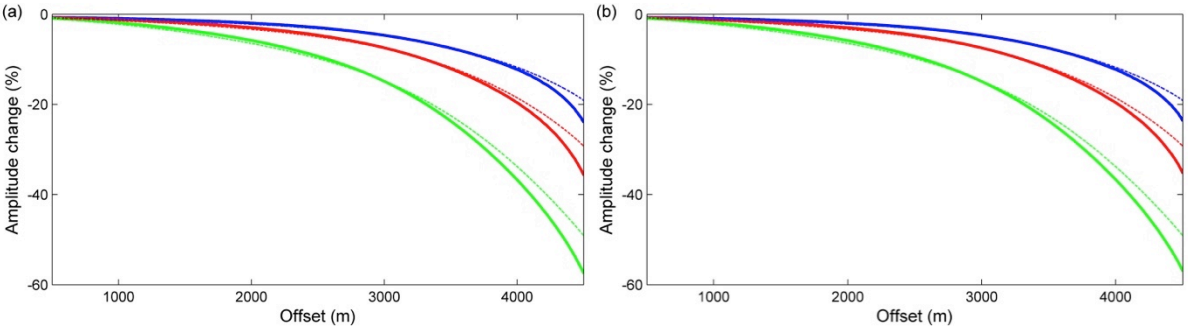

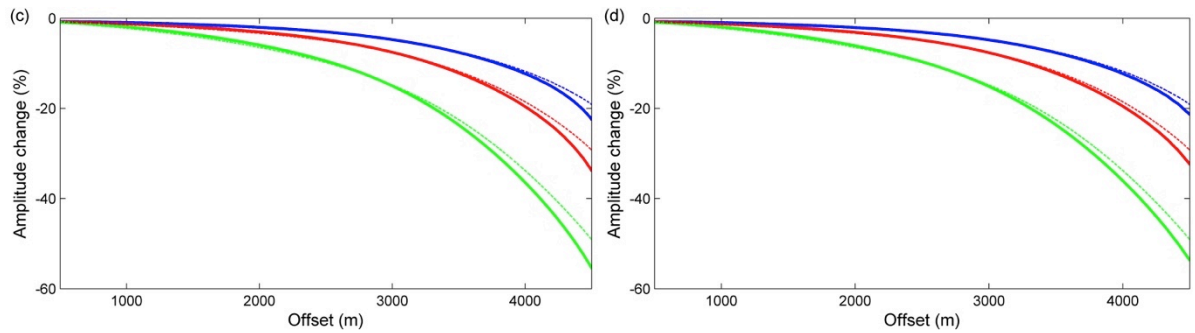

Figure 6. Time-lapse changes in P-P wave reflection coefficients due to the modelled induced velocity anisotropy calculated with respect to the baseline isotropic model at four azimuths: (a) $\phi = 0^o$, (b) $\phi = 30^o$, (c) $\phi = 60^o$, and (d) $\phi = 90^o$. The dotted-thin curves represent the measurements for the flat horizon model and the solid-thick curves represent the measurements for the dipping horizon model. The reflection amplitude changes from the isotropic model are: blue for weak anisotropic (anisotropy1) model, red for moderate anisotropic (anisotropy2) model and green for strong anisotropic (anisotropy3) model.

In Figure 6, time-lapse P-P wave AVOA changes due to the induced velocity anisotropy calculated with respect to the baseline isotropic model at four azimuths are compared between theflat and dipping horizon models. It can be seen that the azimuthal variations in the time-lapse reflection amplitude changes for the dipping-layered model are more marked when compared with the flat horizon model at far offsets, whereas at near offsets the changes are indistinguishable.

3.2. Hydro-mechanical graben-style reservoir model

■ Methodology

In this reservoir model, we explore the influence of subsurface geometry on the time-lapse AVO and AVOA response using a graben-structure reservoir geometry consisting of three reservoir compartments separated by two normal faults (see Angus et al. 2010). Numerical hydro-mechanical simulation is applied to the geometry to predict the influence of fluid extraction on the elastic properties of the reservoir system, specifically the time-lapse reflection amplitude response. Two production cases are examined, one where the faults have high fluid-flow transmissibility (i.e., the faults are not barriers to fluid flow, HFT) and one where the faults have low fluid-flow transmissibility (i.e., the faults act as fluid flow barriers, LFT). The hydro-mechanical simulations are performed using a two-way iteratively coupled approach (Segura et al. 2011) linking the reservoir flow simulator

Tempest with the geomechanical solver Elfen. In this coupled approach the geomechanical simulator uses the pore pressure evolution calculated in the reservoir simulator to update the geomechanical loading, and the reservoir simulator uses the updated pore volume calculated in the geomechanical simulator to update the fluid-flow properties. Due to the 3D geometry,it is expected that fluid extraction within the two-fault graben reservoir model will yield fully triaxial stress perturbations and hence seismic anisotropy will develop (e.g., Herwanger and Koutsabeloulis 2011). Monitoring the effective stress and reservoir pore pressure evolution across the faults and within the compartments is therefore of considerable significance to improve hydrocarbon extraction strategies as well as avert drilling and depletion related geomechanical problems. Thus this model is of practical significance because it will allow us to examine whether time-lapse AVO and AVOA analysis can be used to monitor reservoir compartmentalization.

For both the high (HFT) and low (LFT) flow transmissibility cases, the outputs from the hydro-mechanical simulations are used to construct dynamic elastic models (i.e., elasticity suitable for seismic frequencies) for the anisotropic ray tracing (see Angus et al. 2011). Three elastic models are generated: an isotropic baseline model and two generally anisotropic monitor models (monitor1 for five years of depletion and monitor2 for ten years of depletion). The monitor models are anisotropic due to the evolution of the triaxial effective stress field during fluid extraction. The seismic anisotropy is predicted based on the stress-sensitive microcrack rock physics transform of Verdon et al. (2008) (see Appendix A for descriptions of dynamic elasticity construction from the output of hydro-mechanical simulations using the microcrack rock physics model). In order to examine the influence of induced velocity heterogeneity and induced velocity anisotropy due to reservoir depletion on the time-lapse seismic amplitude response, time-lapse isotropic and anisotropic elastic models are considered.

There are eight distinct symmetry classes for anisotropic media: triclinic, monoclinic, orthorhombic, tetragonal, trigonal, hexagonal, cubic and isotropic (e.g., Babuska and Cara 1991; Liu and Martinez 2012). Browaeys and Chevrot (2004) show that a given vector T belonging to any anisotropic symmetry class can be decomposed into a sum of anisotropic components belonging to the eight elastic symmetry groups

$$T = T_{tric} + T_{mon} + T_{ort} + T_{tet} + T_{trig} + T_{hex} + T_{cub} + T_{iso}, \quad (6)$$

where T_{tric}, T_{mon}, T_{ort}, T_{tet}, T_{trig}, T_{hex}, T_{cub} and T_{iso} are elastic vectors belonging to the triclinic, monoclinic, orthorhombic, tetragonal, trigonal, hexagonal, cubic and isotropic elastic symmetry classes, respectively. This formulation allows any generally anisotropic elastic tensor to be approximated by an optimal hexagonal (i.e., TI) elastic medium, consisting of an isotropic part T_{iso} and an hexagonal part T_{hex}, reducing the number of independent elastic parameters from 21 to 5 using Thomsen (1986) anisotropy parameters.

In the time-lapse isotropic case, it is assumed that no velocity anisotropy is induced and only isotropic velocity changes occur. In the time-lapse anisotropic case, the development of velocity heterogeneity occurs, but where induced velocity anisotropy also develops. For both the isotropic and anisotropic cases, the initial baseline elastic model is isotropic (V_{iso1}). For the isotropic time-lapse case, an isotropic equivalent monitor elastic model is derived from the anisotropic modelassuming only vertical effective stress changes (i.e., uniaxial strain), and hence the elastic tensor components C_{33} and C_{44} are used to compute the P- and S-wave velocities (V_{iso2}), respectively. Based on the decomposition approach of Browaeys and Chevrot (2004), the induced anisotropic elasticity calculated using the hydro-mechanical simulations is approximated to TI anisotropy, allowing the induced anisotropy to be characterised by Thomsen (1986) anisotropy parameters suitable to be used in equations (3)-(5). The Thomsen (1986) anisotropy parameters approximated for the anisotropic model (V_{aniso}) of monitor1 within the reservoir are: $\varepsilon = 0.16$, $\gamma = 0.10$ and $\delta = 0.01$ for the HFT model, and $\varepsilon = -0.02$, $\gamma = -0.01$ and $\delta = -0.01$ for the LFT model.

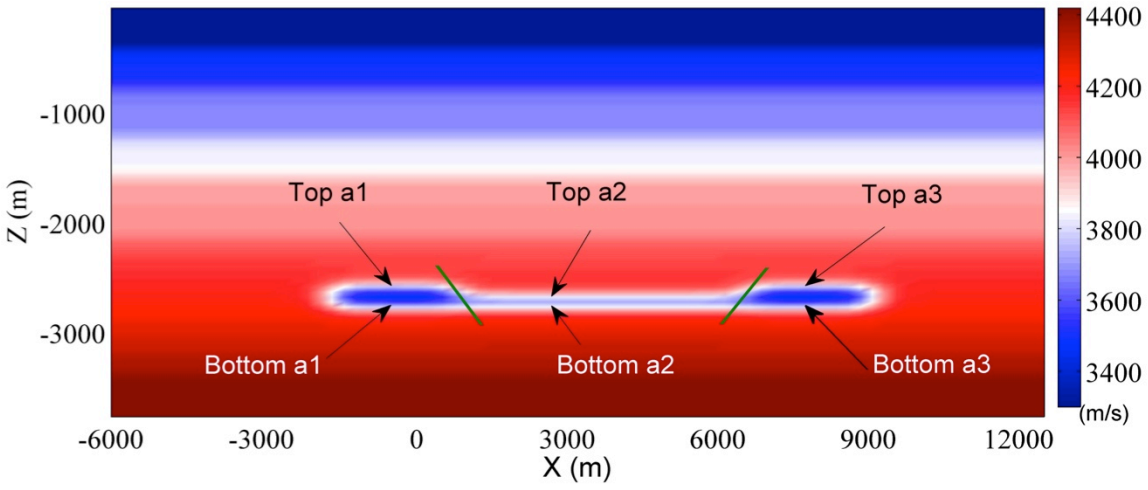

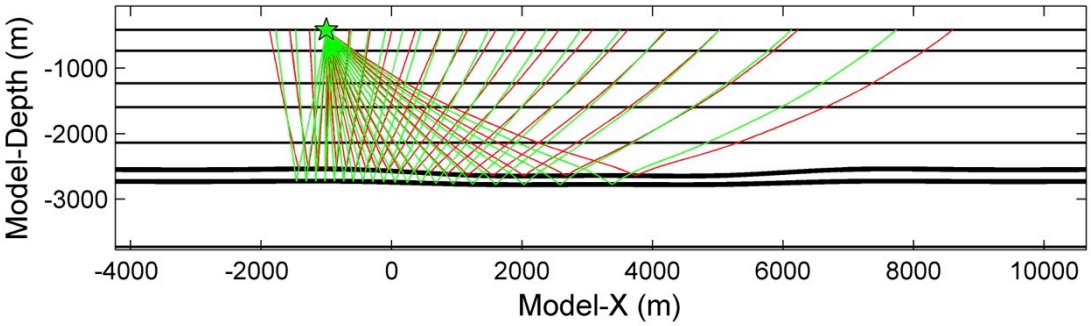

Figure 7. Top: Baseline P-wave velocity vertical section (X-Z) through the middle of the graben reservoir model (see Angus et al. 2010). The six arrows represent locations within the model where the elastic parameters are taken for Table 1. The two green lines represent the locations of the normal faults. Bottom: Example of rays traced through the graben reservoir model and reflected from two interfaces; the top and base reservoir reflected rays are indicated by the red and green lines respectively, from a source at X=-1000 m. The thin layer between the two interfaces (thick-black horizons) is the producing reservoir.

As was done in the previous section, we use the anisotropic ray tracer ATRAK to calculate the reflection amplitudes for different azimuths. The influence of induced isotropic velocity heterogeneity (i.e., V_{iso1} to V_{iso2}) and induced seismic anisotropy (i.e., V_{iso1} to V_{aniso}) is investigated for both the P-P and P-S waves. Figure 7 shows an example of P-P rays traced through the graben reservoir model from a common source-point (X=-1000 m) and tracking reflections from two interfaces (i.e., the top and the bottom reservoir horizons). Since we are concerned with evaluating the changes within the producing reservoir, only the rays reflected from the bottom reservoir interface are investigated.

■ Results

Figure 8 displays the time-lapse seismic changes in reflection coefficients calculated between the isotropic baseline (V_{iso1}) and the induced isotropic monitor1 (V_{iso2}) and anisotropic monitor1 (V_{aniso}) HFT and LFT models at four azimuths for P-P and P-S_1 waves, respectively. It can be seen that the impact of induced velocity heterogeneity and anisotropy is noticeable on the P-P reflection coefficients changes for all azimuths, and the changes in P-P reflection coefficients decrease with increasing offset. There are observable differences in reflection amplitude changes (~5%) for P-P wave between the induced isotropic and induced anisotropic models and this indicates that it is important to include the influence of induced anisotropy. The azimuthal variation is related to the geometry, where the

influence of the fault along azimuth $\phi = 0^o$ differs from the influence of the reservoir edges along the other azimuths $\phi = 30^o$, $\phi = 60^o$ and $\phi = 90^o$. The azimuthal variation suggests that the reservoir is not undergoing uniaxial deformation and this is expected since the reservoir does not have infinite extent. It is important to note that the P-P and P-S_1 waves show different offset dependence as well as sign in reflection amplitude changes (negative for P-P and positive for P-S_1). In addition, the time-lapse reflection amplitude changes for the P-P waves are much larger than that of the P-S_1 waves. For the LFT model, there is significantly less azimuthal variation in P-P reflection coefficients due to reservoir geometry, whereas there appears to be an increased sensitivity in the P-S reflection coefficient especially for the 90^0 azimuth.

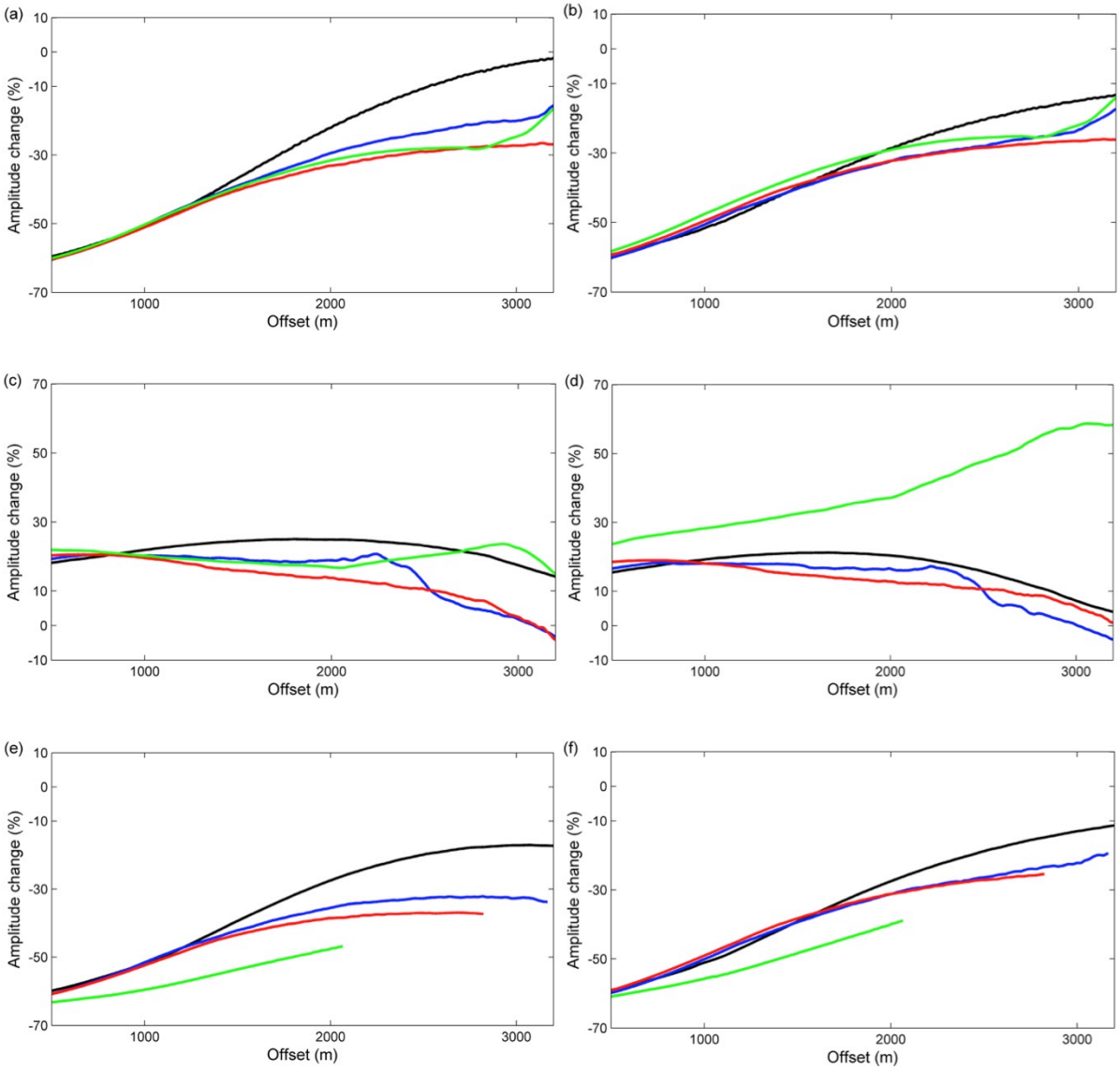

Figure 8. Time-lapse changes in reflection amplitudes for P-P and P-S_1 waves for the 5 year monitor (monitor1) HFT (left) and LFT (right) graben reservoir model. Panels (a), (b), (c) and (d) assume isotropic (V_{iso2}) changes, and panels (e) and (f) assume anisotropic (V_{aniso}) changes in elasticity at four azimuths: $\phi = 0^o$ (black curve), $\phi = 30^o$ (blue curve), $\phi = 60^o$ (red curve) and $\phi = 90^o$ (green curve). Panels (a), (b), (e) and (f) represent P-P wave results, and panels (c) and (d) represent P-S_1 wave results.

(a)

Parameter / Model	α (km/s)	β (km/s)	ρ (g/cm3)	ε	γ	δ
Top a1	4.183	1.261	2.7	0	0	0
	3.364	1.942	2.7	0	0	0
Top a2	4.195	1.265	2.7	0	0	0
	3.375	1.949	2.7	0	0	0
Top a3	4.183	1.261	2.7	0	0	0
	3.364	1.942	2.7	0	0	0
Bottom a1	3.377	1.950	2.7	0	0	0
	4.232	1.276	2.7	0	0	0
Bottom a2	3.375	1.949	2.7	0	0	0
	4.246	1.280	2.7	0	0	0
Bottom a3	3.377	1.950	2.7	0	0	0
	4.232	1.276	2.7	0	0	0

(b)

Parameter / Model	α (km/s)	β (km/s)	ρ (g/cm3)	ε	γ	δ
Top a1	4.021	1.257	2.7	-0.01	0	-0.01
	3.759	2.095	2.7	0.17	0.06	0.17
Top a2	4.124	1.263	2.7	0	0	0
	3.832	2.119	2.7	0.19	0.06	0.2
Top a3	4.110	1.259	2.7	0	0	0
	3.708	2.082	2.7	0.16	0.05	0.16
Bottom a1	3.773	2.102	2.7	0.17	0.06	0.17
	4.086	1.272	2.7	0	0	0
Bottom a2	3.832	2.119	2.7	0.19	0.06	0.2
	4.136	1.278	2.7	-0.01	0	-0.01
Bottom a3	3.696	2.081	2.7	0.14	0.05	0.14
	4.146	1.274	2.7	0	0	0

(c)

Parameter / Model	α (km/s)	β (km/s)	ρ (g/cm3)	ε	γ	δ
Top a1	3.910	1.254	2.7	-0.01	0	-0.01
	3.834	2.112	2.7	0.19	0.06	0.19
Top a2	4.028	1.260	2.7	-0.01	0	-0.01
	3.949	2.144	2.7	0.21	0.07	0.22
Top a3	3.960	1.256	2.7	-0.01	0	-0.01
	3.817	2.108	2.7	0.18	0.06	0.19
Bottom a1	3.852	2.120	2.7	0.19	0.06	0.19
	4.023	1.271	2.7	-0.01	0	-0.01
Bottom a2	3.949	2.144	2.7	0.21	0.07	0.22
	4.086	1.277	2.7	-0.01	0	-0.01
Bottom a3	3.834	2.116	2.7	0.18	0.06	0.18
	4.094	1.272	2.7	0	0	0

(d)

Parameter / Model	α (km/s)	β (km/s)	ρ (g/cm3)	ε	γ	δ
Top a1	3.944	1.255	2.7	-0.01	0	-0.01
	3.364	1.942	2.7	0	0	0
Top a2	4.267	1.266	2.7	0	0	0
	3.375	1.949	2.7	0	0	0
Top a3	4.222	1.262	2.7	0	0	0
	3.364	1.942	2.7	0	0	0
Bottom a1	3.377	1.950	2.7	0	0	0
	3.983	1.269	2.7	-0.01	0	-0.01
Bottom a2	3.375	1.949	2.7	0	0	0
	4.359	1.282	2.7	0.01	0	0.01
Bottom a3	3.377	1.950	2.7	0	0	0
	4.267	1.276	2.7	0	0	0

(e)

Parameter / Model	α (km/s)	β (km/s)	ρ (g/cm3)	ε	γ	δ
Top a1	3.569	1.242	2.7	-0.03	-0.01	-0.03
	3.364	1.942	2.7	0	0	0
Top a2	4.280	1.267	2.7	0	0	0
	3.375	1.949	2.7	0	0	0
Top a3	4.224	1.262	2.7	0	0	0
	3.364	1.942	2.7	0	0	0
Bottom a1	3.377	1.950	2.7	0	0	0
	3.731	1.259	2.7	-0.01	0	-0.01
Bottom a2	3.375	1.949	2.7	0	0	0
	4.380	1.283	2.7	0	0	0
Bottom a3	3.377	1.950	2.7	0	0	0
	4.267	1.276	2.7	0	0	0

Table 1 The elastic parameters calculated at three locations along the top and bottom reservoir horizons; the lateral locations are a1=-711 m, a2=2714 m and a3=7120 m. These values are extracted from the output of the hydro-mechanical simulations for the (a) baseline, (b) and (d) monitor survey after 5 years of production (monitor1) and (c) and (e) monitor survey after 10 years of production (monitor2). Where (b) and (c) are for the HFT reservoir models, and (d) and (e) are for the LFT reservoir models. In this table, α and β are the vertical P- and S-wave velocities respectively, ρ is the bulk density, and ε, γ and δ are the Thomsen (1986) anisotropy parameters.

To gain some physical insight into the approximate AVO and AVOA equations (1)-(5), we extract elastic properties across the top and bottom reservoir horizons at three lateral locations: -711 m, 2714 m and 7120 m. These three points are shown in Figure 7 and represent the central horizon point of each compartment. The values in Table 1 are given for the baseline, monitor1 and monitor2 elastic models for the high and low fluid-flow fault transmissibility cases. The elasticity values are then used to compute the approximate time-lapse AVO and AVOA responses within each reservoir compartment.

In Figure 9, reservoir depletion induced seismic anisotropy (due to triaxial changes in the stress state) is illustrated for a specific location within the center of the middle reservoir compartment in the middle of the layer (X=4000 m) for the HFT models. Figure 9 shows horizontal and vertical cross-sections of the slowness and group velocity surfaces of the P-, S_1- and S_2-waves for the baseline and 5 year monitor (monitor1) models. Since the baseline model is isotropic, the slowness and group

velocity surfaces are circular and only one shear-wave exists. For the horizontal sections, there is an increase in P- and S-wave velocity as well as the development of fast and slow S-waves. However, the surfaces are more or less circular indicating very weak azimuthal anisotropy. For the vertical sections, there is an increase in P- and S-wave velocity as well as the development of shear-wave splitting as the direction of wave propagation moves from vertical to horizontal (typical of VTI symmetry). These results indicate uniaxial deformation due to a larger effective stress change occurring in the vertical direction than in the horizontal direction, which is expected for this central region of the middle compartment.

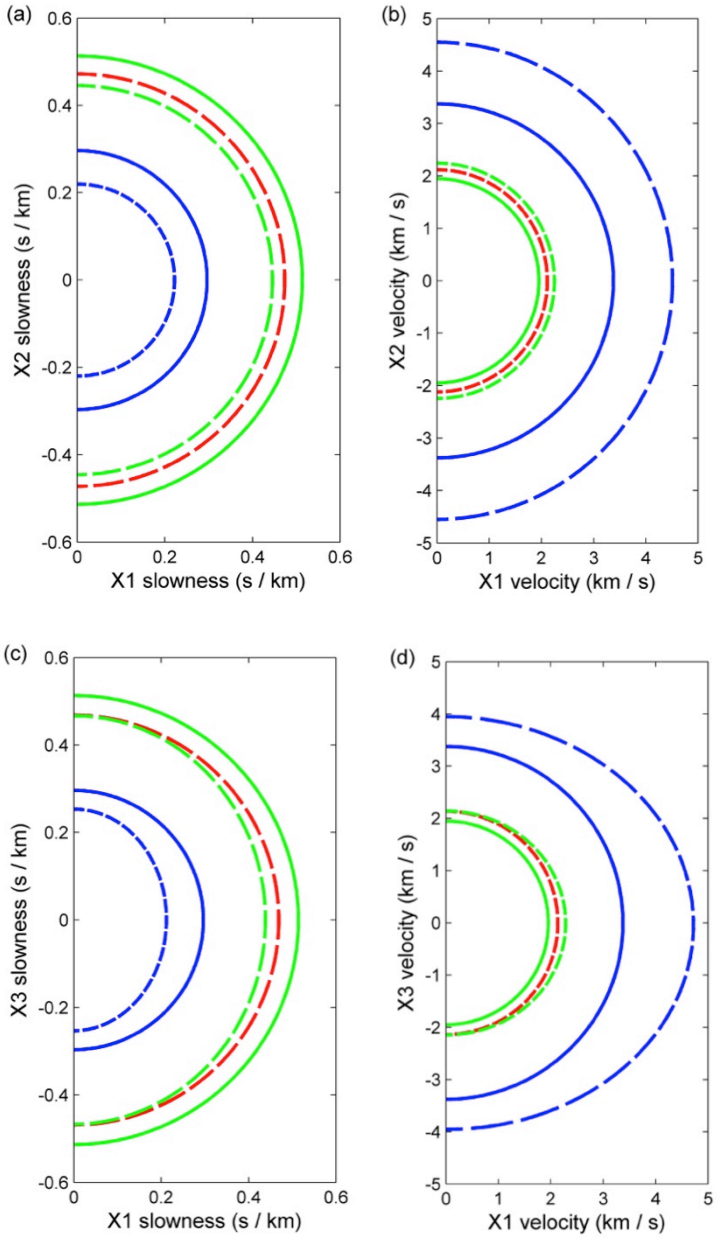

Figure 9. Shown are the slowness and group velocity surfaces for the HFT graben reservoir model for the baseline isotropic elastic tensor and the induced anisotropic elastic tensor after 5 years of production (monitor1) within the middle reservoir compartment (X=4000 m): (top) horizontal cross-section and (bottom) vertical cross-section. The solid curve represents the baseline model and the dashed curve represents the 5 year monitor model; blue for the P-wave, red for the fast S_1-wave and green for the slow S_2-wave.

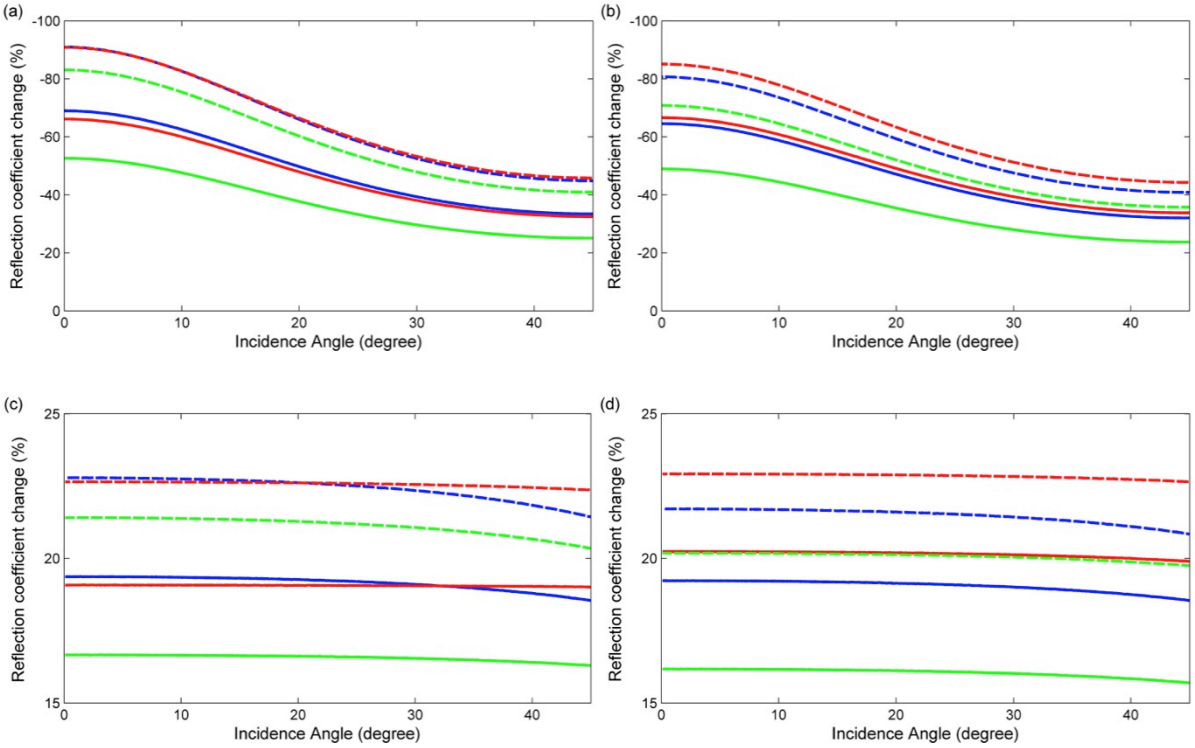

Figure 10. Time-lapse changes in P-P (a and b) and P-S (c and d) AVO response calculated with respect to the isotropic baseline model assuming only isotropic changes in elasticity for the HFT graben reservoir model. The left column represents the top horizon and the right column represents the bottom horizon. The blue curve is the AVO response change for point a1, the red curve for point 2 and green curve for point 3. The solid curve is reflection coefficient change for the 5 year monitor (monitor1) model and dashed curve for the 10 year monitor (monitor2) model.

For the model where only induced isotropic changes in elastic properties occur, the time-lapse P-P AVO response change between the baseline and monitor1, and baseline and monitor2 HFT models is more sensitive than the P-S AVO response change on both the top and bottom reservoir interfaces for the selected locations. In Figure 10, the time-lapse changes in the P-P AVO curves (using equation 1) are on the order of 50% to 90%, whereas the time-lapse changes in the P-S AVO curves (using

equation 2) are much smaller (i.e., 16% to 22%). However, the time-lapse changes in the P-P and P-S AVO response have differing signs and so this could potentially be an indication of reservoir/pressure compartmentalization related to fluid properties and pore pressure modifications.

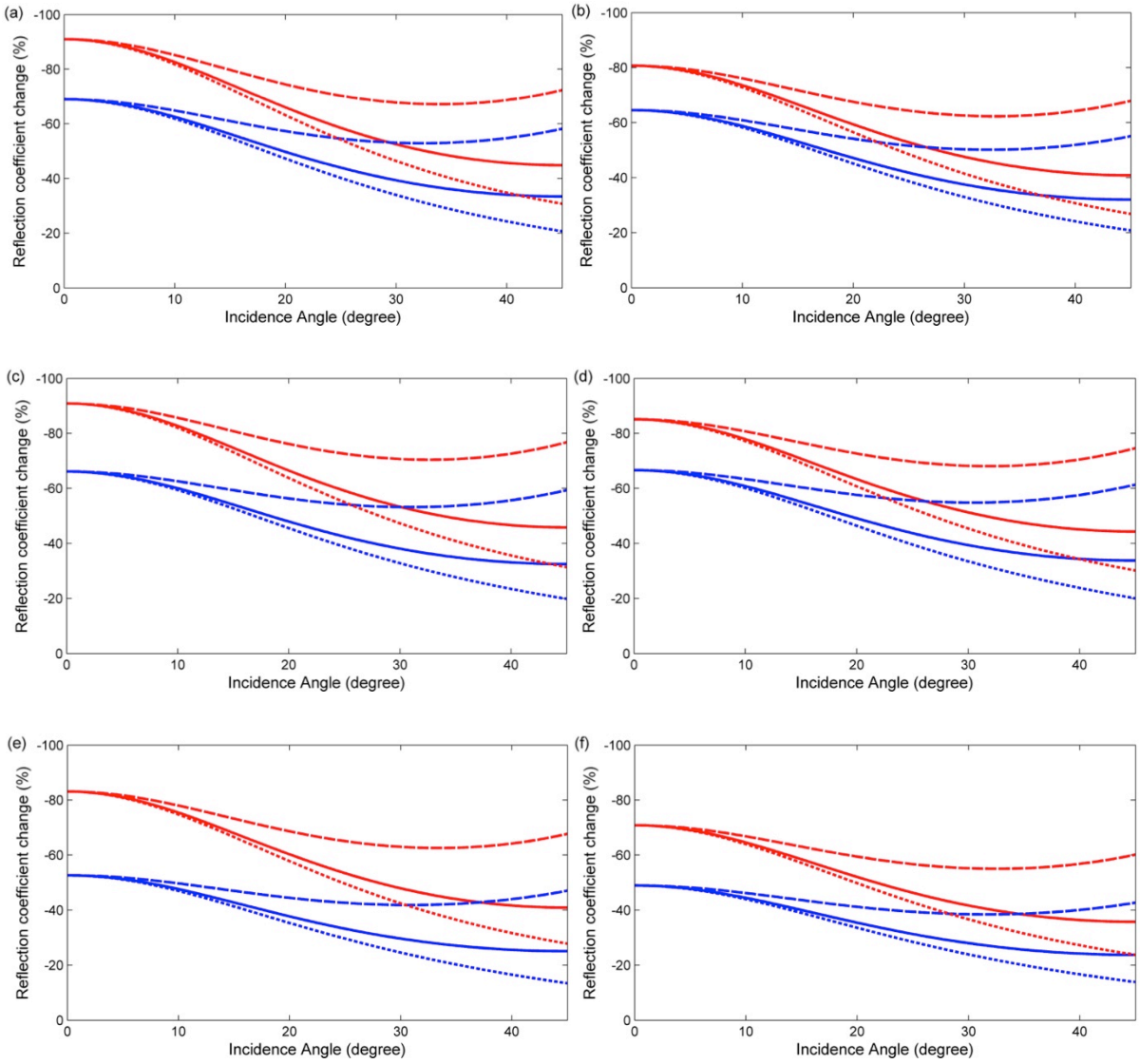

Figure 11. Time-lapse changes in P-P AVO response calculated with respect to the isotropic baseline model for the induced isotropic and anisotropic changes in elasticity for the HFT graben reservoir model. The left column represents the top horizon and the right column represents the bottom horizon. The top row represents the AVO response change for point a1, the middle for point a2 and the bottom for point a3. The solid curve represents the induced isotropic model AVO response, the dashed curve represents the induced anisotropic model with VTI symmetry and the dotted curve represents the induced anistropic model with HTI symmetry, with blue for the 5 year monitor (monitor1) model and red for the 10 year monitor (monitor2) model.

For the model where induced anisotropic changes in the elastic properties occur, we explore the signature of VTI and HTI caused by reservoir pressure depletion. In Figure 11, the time-lapse changes in P-P AVO curves are compared for isotropic, VTI and HTI changes for two monitor (monitor1 and monitor2) models of HFT calculated respect to the isotropic baseline model, where the VTI response is computed using equation (3) and for HTI using equation (4). Time-lapse AVO changes increase with reservoir fluid extraction. Both the VTI and HTI cases produce significantly different responses to that of the isotropic case. In all cases the time-lapse AVO changes are all negative and decline with increasing incidence angle. While the time-lapse AVO changes for HTI are smaller than that of the isotropic model, the results for VTI are much larger than the isotropic model. In monitor1, the time-lapse AVO changes have similar magnitude (i.e., ±5% differences) for the top and the bottom reservoir horizons. In monitor2 the time-lapse AVO changes for the top and the bottom reservoir horizons can differ by up to ±13%. This might be indicative of the greater influence of reservoir compaction due to increasing effective stress within the producing reservoir being larger than the overburden and underburden extension (e.g., Sayers 2010).

Figure 12 displays the time-lapse changes in P-P AVOA due to induced HTI anisotropy (equation 4) for the top and bottom reservoir horizons between the baseline and monitor1, and baseline and monitor2 models at the three lateral locations (a1, a2 and a3) using the elastic parameters in Table 1 for the HFT model. Fluid depletion induced HTI anisotropy produces different AVOA responses at the selected locations. It can be noted that time-lapse AVOA changes range from -90% to -15% for increasing incidence angles (i.e., 0^o to 45^o). As well, the time-lapse AVO changes with azimuth (i.e., 0^o to 90^o) are significant, especially for incidence angles larger than 30^o.

1

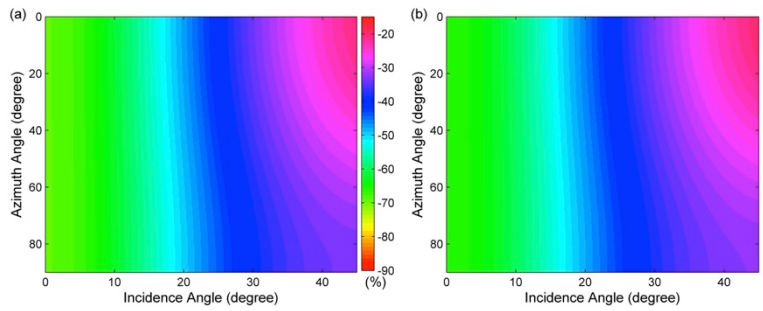
(a)
(b)
Azimuth Angle (degree)
Incidence Angle (degree)
0
20
40
60
80
0
10
20
30
40
-20
-30
-40
-50
-60
-70
-80
-90
(%)

2

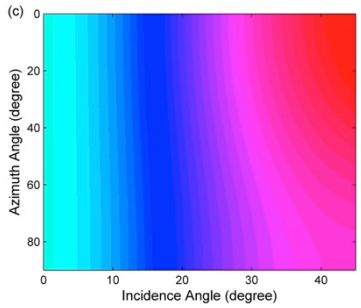
(c)
Azimuth Angle (degree)
Incidence Angle (degree)
0
20
40
60
80
0
10
20
30
40

3

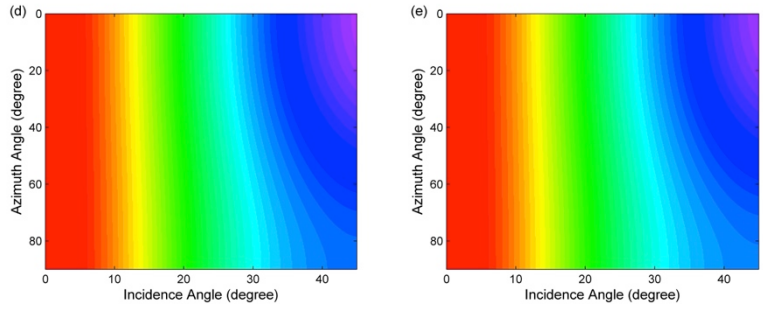
(d)
(e)
Azimuth Angle (degree)
Incidence Angle (degree)
0
20
40
60
80
0
10
20
30
40

4

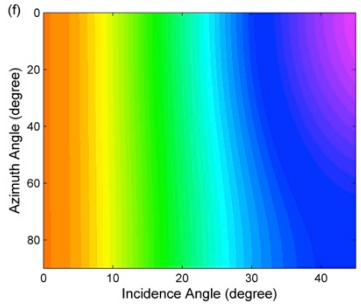
(f)
Azimuth Angle (degree)
Incidence Angle (degree)
0
20
40
60
80
0
10
20
30
40

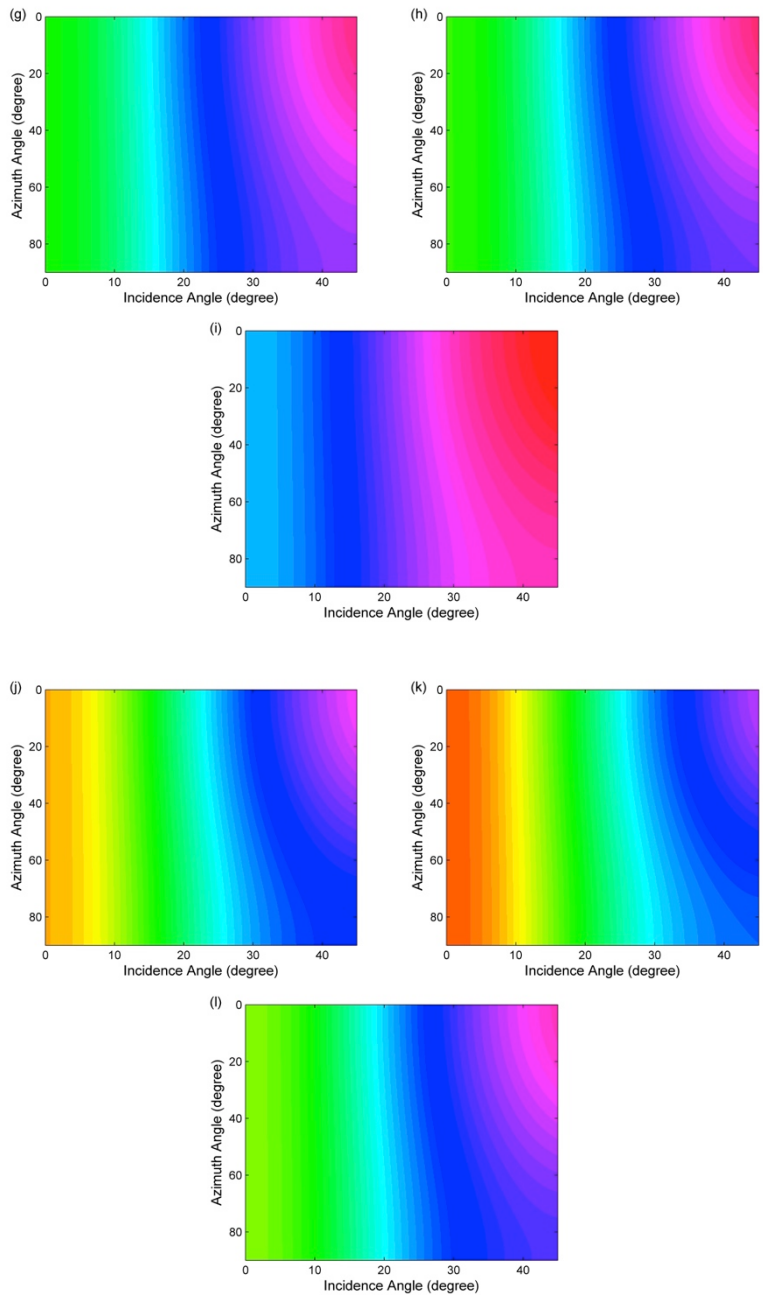

Figure 12. Time-lapse changes in P-P AVOA response calculated with respect to the isotropic baseline model for the induced anisotropic changes in elasticity for the HFT graben reservoir model. The top two rows represent the top reservoir horizon and the bottom two rows represent the bottom reservoir horizon. The left column represents the AVOA response change for point a1, the middle column for point a2 and the right column for point a3. The first and third rows are AVOA response change for the 5 year monitor (monitor1) model and the second and bottom rows for the 10 year monitor (monitor2) model.

Parameter / Model	A	G_{iso}	G_{aniso}
Baseline a1	-0.1085	-0.4016	0
Baseline a2	-0.1083	-0.4019	0
Baseline a3	-0.1085	-0.4016	0
Mon1(HFT) a1	-0.0337	-0.3831	-0.0240
Mon1(HFT) a2	-0.0367	-0.3806	-0.0231
Mon1(HFT) a3	-0.0514	-0.3907	-0.0241
Mon2(HFT) a1	-0.0098	-0.3716	-0.0286
Mon2(HFT) a2	-0.0099	-0.3643	-0.0259
Mon2(HFT) a3	-0.0184	-0.3746	-0.0240
Mon1(LFT) a1	-0.0794	-0.3938	-0.0051
Mon1(LFT) a2	-0.1167	-0.4045	0
Mon1(LFT) a3	-0.1131	-0.4029	0
Mon2(LFT) a1	-0.0296	-0.3834	-0.0075
Mon2(LFT) a2	-0.1182	-0.4048	0
Mon2(LFT) a3	-0.1133	-0.4030	0

Parameter / Model	A	G_{iso}	G_{aniso}
Baseline a1	0.1124	0.4002	0
Baseline a2	0.1143	0.3996	0
Baseline a3	0.1124	0.4002	0
Mon1(HFT) a1	0.0398	0.3819	0.0192
Mon1(HFT) a2	0.0382	0.3773	0.0280
Mon1(HFT) a3	0.0574	0.3903	0.0181
Mon2(HFT) a1	0.0217	0.3712	0.0294
Mon2(HFT) a2	0.0171	0.3624	0.0261
Mon2(HFT) a3	0.0328	0.3755	0.0223
Mon1(LFT) a1	0.0823	0.3922	0.0051
Mon1(LFT) a2	0.1272	0.4037	-0.0049
Mon1(LFT) a3	0.1164	0.4017	0
Mon2(LFT) a1	0.0823	0.3922	0.0051
Mon2(LFT) a2	0.1272	0.4037	-0.0049
Mon2(LFT) a3	0.1164	0.4017	0

Table 2 The AVOA intercept (A) and gradients (G_{iso} and G_{aniso}) calculated on the top horizon (left) and the bottom horizon (right) at three lateral locations (a1, a2 and a3) for the graben-style reservoir models of baseline, monitor1 and monitor2 having high (HFT) and low (LFT) fluid-flow fault transmissibility.

Azimuth / Model	0°	30°	60°	90°
Baseline a1	-0.4016	-0.4016	-0.4016	-0.4016
Baseline a2	-0.4019	-0.4019	-0.4019	-0.4019
Baseline a3	-0.4016	-0.4016	-0.4016	-0.4016
Mon1(HFT) a1	-0.4071	-0.4011	-0.3891	-0.3831
Mon1(HFT) a2	-0.4037	-0.3979	-0.3863	-0.3806
Mon1(HFT) a3	-0.4148	-0.4088	-0.3967	-0.3907
Mon2(HFT) a1	-0.4002	-0.3930	-0.3787	-0.3716
Mon2(HFT) a2	-0.3902	-0.3837	-0.3708	-0.3643
Mon2(HFT) a3	-0.3986	-0.3926	-0.3806	-0.3746
Mon1(LFT) a1	-0.3989	-0.3977	-0.3951	-0.3938
Mon1(LFT) a2	-0.4045	-0.4045	-0.4045	-0.4045
Mon1(LFT) a3	-0.4029	-0.4029	-0.4029	-0.4029
Mon2(LFT) a1	-0.3909	-0.3891	-0.3853	-0.3834
Mon2(LFT) a2	-0.4048	-0.4048	-0.4048	-0.4048
Mon2(LFT) a3	-0.4030	-0.4030	-0.4030	-0.4030

Azimuth / Model	0°	30°	60°	90°
Baseline a1	0.4002	0.4002	0.4002	0.4002
Baseline a2	0.3996	0.3996	0.3996	0.3996
Baseline a3	0.4002	0.4002	0.4002	0.4002
Mon1(HFT) a1	0.4011	0.3962	0.3866	0.3819
Mon1(HFT) a2	0.4053	0.3983	0.3843	0.3774
Mon1(HFT) a3	0.4084	0.4039	0.3948	0.3903
Mon2(HFT) a1	0.4006	0.3933	0.3785	0.3712
Mon2(HFT) a2	0.3885	0.382	0.3689	0.3624
Mon2(HFT) a3	0.3978	0.3922	0.3811	0.3755
Mon1(LFT) a1	0.3973	0.3960	0.3935	0.3922
Mon1(LFT) a2	0.3988	0.4000	0.4025	0.4037
Mon1(LFT) a3	0.4017	0.4017	0.4017	0.4017
Mon2(LFT) a1	0.3905	0.3892	0.3866	0.3854
Mon2(LFT) a2	0.4043	0.4043	0.4043	0.4043
Mon2(LFT) a3	0.4017	0.4017	0.4017	0.4017

Table 3 The AVOA gradients versus azimuths $G_{iso}+G_{aniso}\cos^2\phi$ ($\phi = 0^o$, 30^o, 60^o and 90^o) for the top horizon (left) and the bottom horizon (right) at three lateral locations (a1, a2 and a3) for the graben-style reservoir models of baseline, monitor1 and monitor2 having high (HFT) and low (LFT) fluid-flow fault transmissibility.

The AVOA intercept A and gradients G_{iso} and G_{aniso} are calculated using equation (5) for the top and bottom reservoir horizons at the three lateral locations in the HFT and LFT reservoir models (see Table 2). For low to moderate source-receiver offset, the P-P AVOA gradient variation $G_{iso} + G_{aniso}\cos^2\phi$ with azimuths $\phi = 0^o$, 30^o, 60^o and 90^o for the top and bottom reservoir horizons for the baseline, monitor1 and monitor2 models are shownin Table 3. In HFT models, as the azimuth increases the AVOA gradients decrease for both monitor1 and monitor2 models, with no variation for the baseline model as expected. The estimates for the top and bottom horizons have opposing signs (i.e., negative for the top horizonand positive for the bottom horizon). While the gradients within the two end compartmentsare similar, the gradients in the middle compartment are smaller. This suggests different effective stress states within these compartments due to reservoir geometry and stress arching (see Angus et al. 2010). In LFT models, as the azimuth increases the AVOA gradients decrease for both monitor1 and monitor2 models at the left producing compartment and are constant for the middle and right compartments, except for the monitot1 model at bottom horizon where the AVOA gradients increase with increasing azimuth. This indicates that the major effective stress changes are constrained to the left compartment, and none (or negligible) induced effective stress changes occur across the faults due to low fluid-flow transmissibility (i.e., reservoir compartmentalization).

In general, P-P AVOA analysis has been used extensively to characterise *in situ* fracture networks (e.g., Hall and Kendall 2003; Shams and MacBeth 2003). However, there have been studies where the AVOA technique has been used as a time-lapse seismic attribute to monitor reservoir compartmentalization and fluid-flow (e.g., Hall and MacBeth 2001). Angus et al. (2013) and Angus et al. (2015) make the first attempt at linking field measurements of AVOA with hydro-mechanical simulation, yielding reasonable first-order matches for several horizons.

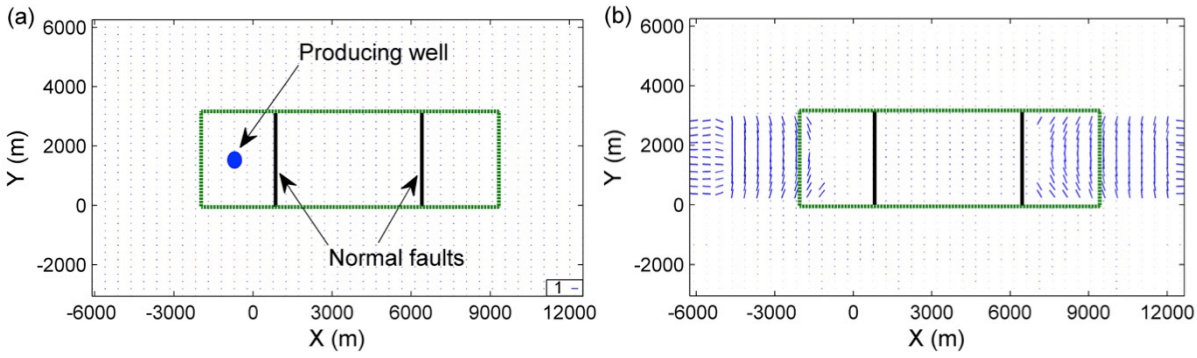

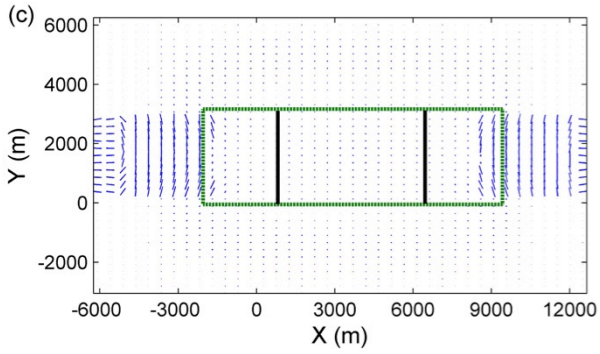

Figure 13. The predicted AVOA response for the top horizon of the high fluid-flow fault transmissibility graben reservoir model calculated from the output of the hydro-mechanical simulation for the (a) baseline, (b) monitor1 and (c) monitor2 cases. The three reservoir compartments are subdivided by the two normal faults (two black lines). The producing well (defined by a blue dot) is situated in the left compartment. In this Figure and Figure 14, the sticks represent the fast direction of the P-wave anisotropy.

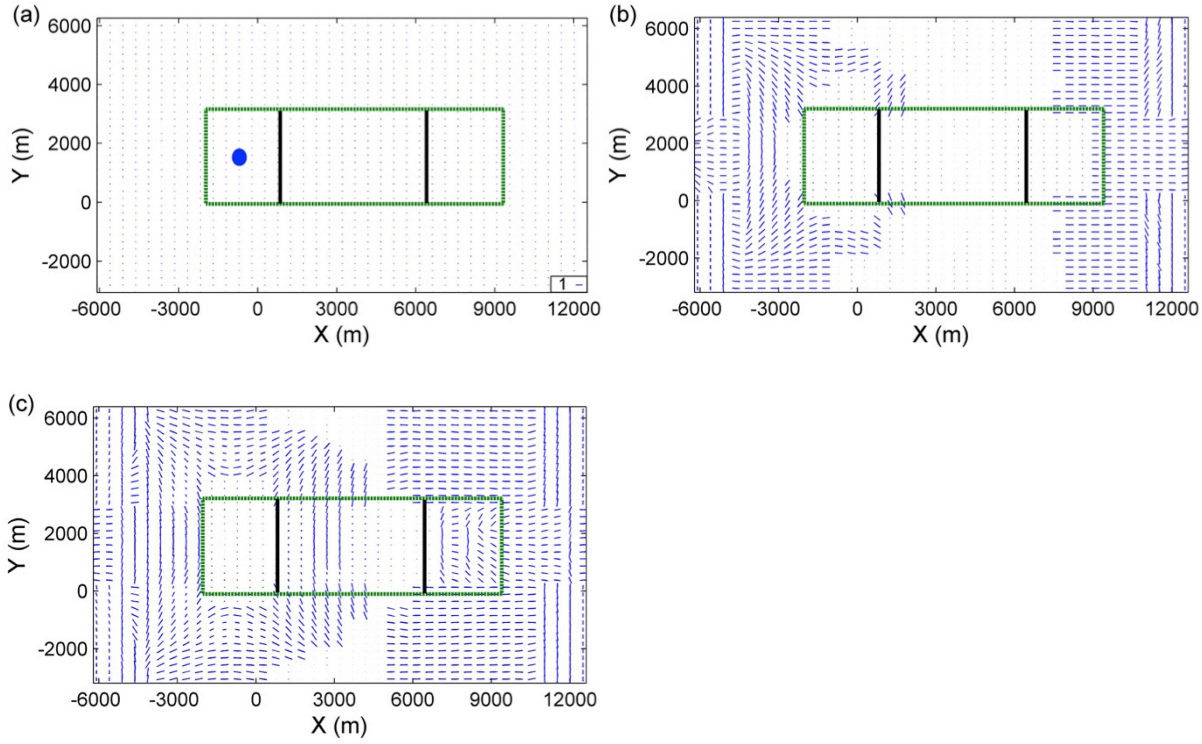

Figure 14. The predicted AVOA response for the top horizon of the low fluid-flow fault transmissibility graben reservoir model calculated from the output of the hydro-mechanical simulation for the (a) baseline, (b) monitor1 and (c) monitor2 cases. The three reservoir compartments are subdivided by the two normal faults (two black lines).

In Figures 13 and 14, the AVOA response calculated using the output from the hydro-mechanical graben reservoir model is shown for the top reservoir horizon for the HFT and the LFT models, respectively. It should be noted that we only display the fast anisotropy direction and not the AVOA magnitude. To predict the AVOA response, we calculate the complex valued reflection coefficients using an anisotropic layer-matrix approach (e.g., see Angus & Thomson 2012 for description of the theory). The reflection coefficient of any interface between two layers is evaluated using the elasticity tensor of the upper and lower layer, where the algorithm subsequently provides synthetic amplitudes at specified offsets and azimuths for each grid point along the chosen horizon. It should be stressed that the predicted AVOA response will be sensitive to not only the geometry of the model but also the stress-dependence of the nonlinear rock physics transform. In Figure 13, the AVOA response is shown for the baseline, monitor1 and monitor2 models for the case of high fluid-flow fault transmissibility. For the baseline there is no azimuthal dependence. However, due to reservoir production both the monitor1 and monitor2 models develop induced anisotropy primarily along the outer edges of the reservoir compartments. In Figure 14, the AVOA response is shown for the baseline, monitor1 and monitor2 models for the case of low fluid-flow fault transmissibility. In this example, there is significant heterogeneity in the AVOA pattern, where induced anisotropy develops around the left-hand (i.e., the compartment with the producing well).

4. Discussion and conclusion

In this paper, we explore the impact of reservoir azimuthal anisotropy on time-lapse seismic reflection amplitude changes using anisotropic ray tracing simulation, as well as the exact and approximate reflectivity solutions. Large deviations in reflection amplitude are observed for ray tracing calculations through the models experiencing isotropic and anisotropic induced elasticity changes. The time-lapse amplitude changes for both P-P and P-S waves are significant for the four-layer dipping model and the hydro-mechanical graben-style reservoir model. The results stress the need to suitably compensate for the influence of subsurface structure, such as dipping horizons in an isotropic medium which might lead to ‘false’ azimuthal variations of reflection amplitude similar to that caused by seismic azimuthal anisotropy, prior to apply AVOA technique to analyse time-lapse seismic observations. There are observable differences in reflection amplitude perturbations between the

induced isotropic and induced anisotropic models and this indicates the importance of including the influence of induced anisotropy.

The time-lapse AVO and AVOA signatures, calculated by applying approximate reflectivity formulations and elasticity derived from the hydro-mechanical graben-style reservoir model, indicate noticeable deviations between models experiencing isotropic and anisotropic TI (VTI and HTI) elasticity changes due to triaxial changes in the stress state. It is worth noting that seimic reflection amplitude is sensitive to the pressure and fluids properties perturbations, which can lead to varied AVO responses. For instance, Landrø (2001) and Stovas and Landrø (2005) use the time-lapse AVO technique to discriminate between pressure and fluid saturation changes with some degree of success.

The P-P AVOA predictions show significant time-lapse changes within the graben-style reservoir hydro-mechanical model. The AVOA patterns are consistent with the expected induced seismic anisotropy due to the triaxial changes in effective stress field related to fluid extraction, geomechanical compaction and reservoir compartmentalization. For the HFT model (see Figure 13), although there is observable induced anisotropy on the right compartment (furthest from the producing well), the reservoir compartments display broadly similar characteristics and thus indicate that all compartments are experiencing the same pore pressure reduction (as expected). In other words, the AVOA pattern is consistent with uniaxial deformation, where VTI anisotropy can develop but not azimuthal or HTI anisotropy. For the LFT model (see Figure 14), the AVOA pattern suggests the development of reservoir compartmentalization and also indicates that the reservoir is not experiencing uniaxial deformation but rather a more complicated stress regime. Thus, time-lapse AVOA technique can be applied not only to assess reservoir compartmentalization and fluid flow, but also as an aid in detecting and understanding changes in the stress state as well as calibrate hydro-mechanical models.

Nevertheless, the employed synthetic reservoir models in this study are far less complex for practical utility. For subsurface earth models having more complicated geological settings, discriminating the influence of compaction-induced velocity heterogeneity from that of seismic anisotropy is still difficult. Hence, in the presence of azimuthal velocity variations, time-lapse seismic analysis might be biased if static azimuthal anisotropic velocity variations are not taken into

consideration. However, errors in estimating induced seismic anisotropy from time-lapse measurements may be smaller compared to other sources of time-lapse error, such as survey repeatability.

ACKNOWLEDGEMENTS

We would like to thank the chief editor and the two anonymous reviewers for helpful comments and suggestions to improve the paper. We are grateful to the Seismic Geomechanics Group of University of Leeds for supporting this work. We thank Rockfield Software for access to the geomechanical simulator ELFEN, and Roxar for access to the geological model builder RMS (TEMPEST). Y.-X. He would like to thank the China Scholarship Council and University of Leeds for financial support, and D.A. Angus acknowledges a Research Council UK for financial support.

REFERENCES

Al-Naamani, A., Shams, A., MacBeth, C., 2004. Joint interpretation of isotropic and anisotropic attributes for a Turbidite Reservoir. EAGE 66th Conference & Exhibition, Paris, France, P164.

Angus, D.A., Dutko, M., Kristiansen, T.G., Fisher, Q.J., Kendall, J-M., Baird, A.F., Barkved, O.I., Yu, J., Zhao, S., 2013. Integrated hydro-mechanical and seismic modelling of the Valhall reservoir: A case study of predicting subsidence, AVOA and microseismicity. EAGE 1st International Workshop on Geomechanics and Energy, Lausanne, Switzerland, We-01-04.

Angus, D.A., Kendall, J-M., Fisher, Q.J., Segura, J.M., Skachkov, S., Crook, A.J.L., Dutko, M., 2010. Modelling microseismicity of a producing reservoir from coupled fluid-flow and geomechanical simulation. Geophysical Prospecting 58, 901-914.

Angus, D.A., Dutko, M., Kristiansen, T.G., Fisher, Q.J., Kendall, J.-M., Baird, A.F., Verdon, J.P., Barkved, O.I., Yu, J., Zhao, S., 2015. Integrated hydro-mechanical and seismic modelling of the Valhall reservoir: A case study of predicting subsidence, AVOA and microseismicity. Geomechanics for Energy and the Environment 2, 32-44.

Angus, D.A., Thomson, C.J., 2012. Modelling converted seismic waveforms in isotropic and anisotropic 1-D gradients: discontinuous versus continuous gradient representations. Studia Geophysica et Geodaetica 56, 383-409.

Angus, D.A., Verdon, J.P., Fisher, Q.J., Kendall, J.M., 2009. Exploring trends in microcrack properties of sedimentary rocks: an audit of dry-core velocity-stress measurements. Geophysics 74, E193-E203.

Angus, D.A., Verdon, J.P., Fisher, Q.J., Kendall, J-M., Segura, J.M., Kristiansen, T.G., Crook, A.J.L., Skachkov, S., Yu, J., Dutko, M., 2011. Integrated fluid-flow, geomechanic and seismic modelling for reservoir characterization. Recorder, Canadian Society of Exploration Geophysicists 36(4), 27-36.

Babuska, V., Cara, M., 1991. Seismic anisotropy in the Earth. Dordrecht: Kluwer, ISSN: 978-94-011-3600-6.

Browaeys, J.T., Chevrot, S., 2004. Decomposition of the elastic tensor and geophysical applications. Geophys. J. Int. 156, 667-678.

Calvert, R., 2005. Insights and Methods for 4D Reservoir Monitoring and Characterization. SEG/EAGE Publications, ISBN-13: 978-1560801283.

Crampin, S., 1985. Evidence for aligned cracks in the Earth's crust. First Break 3, 12-15.

Dimri, V.P., Srivastava, R.P., Vedanti, N., 2012. Fractal Models in Exploration Geophysics: Application to Hydrocarbon Reservoirs, p.165. Elsevier Publications, ISBN: 978-0-08-045158-9.

Duxbury, A., White, D., Samson, C., Hall, S.A., Wookey, J., Kendall, J.-M., 2012. Fracture mapping using seismic amplitude variation with offset azimuth analysis at the Weyburn CO_2 storage site. Geophysics 6, N17-N28.

Fryer, G.J., Frazer, L.N., 1984. Seismic waves in stratified anisotropic media. Geophys. J. R. astr. Soc. 78, 691-710.

Garmany, J., 1983. Some properties of elastodynamic eigenousolutions in stratified media. Geophys. J. R. astr. Soc. 75, 565-569.

Gilbert, F., Backus, G., 1966. Propagator matrices in elastic wave and vibration problems. Geophysics 31, 326-332.

Guest, W.S., Kendall, J.M., 1993. Modelling seismic waveforms in anisotropic inhomogeneous media using ray and Maslov asymptotic theory: application to exploration seismology. Canadian Journal of Exploration Geophysics 29(1), 78-92.

Guest, W.S., Thomson, C.J., Spencer, C.P., 1993. Anisotropic reflection and transmission calculations with application to a crustal seismic survey from the East Greenland Shelf. Journal of Geophysical Research 98(B8), 14161-14184.

Hall, S.A., Kendall, J-M., 2003. Fracture characterization at Valhall: Application of P-wave amplitude variation with offset and azimuth (AVOA) analysis to a 3D ocean-bottom data set. Geophysics 68, 1150-1160.

Hall, S.A., MacBeth, C., 2001. AVOA attribute analysis and cross-plotting for time-lapse monitoring of stress and Saturation changes: Application to the Teal South 4D-4C dataset. SEG Annual Meeting, San Antonio, USA, SEG-2001-1619.

He, Y-X., Angus, D.A., Clark, R.A., Hildyard, M.W., 2015(a). Analysis of time-lapse travel-time and amplitude changes to assess reservoir compartmentalization. Geophysical Prospecting, doi: 10.1111/1365-2478.12250.

He, Y.-X., Angus, D.A., Yuan, S.Y., Blanchard, T.D., 2015(b). Time-lapse seismic interpretation in τ-p space using pre-stack data. Journal of Seismic Exploration, in press.

Herwanger, J.V., Horne, S.A., 2009. Linking reservoir geomechanics and time-lapse seismic: Predicting anisotropic velocity changes and seismic attributes. Geophysics 74, W13-W33.

Herwanger, J.V., Koutsabeloulis, N., 2011. Seismic Geomechanics: How to Build and Calibrate Geomechanical Models using 3D and 4D Seismic Data. EAGE Publications, ISBN: 9073834104-9789073834101.

Hudson, J.A., 1980. Overall properties of a cracked solid. Math. Proc. Camb. Phil. Soc. 88, 371-384.

Jenner, E., 2002. Azimuthal AVO: Methodology and data examples. The Leading Edge 21, 782-786.

Jenner, E., Williams, M., 2003. P-wave seismic velocity issues in the presence of azimuthal anisotropy. EAGE 65th Conference & Exhibition, Tunis, Tunisia, E-14.

Jing, C., Rape, T.D., Xu, S., 2006. Sensitivity study of PP and PS AVO azimuthal Anisotropy. SEG Annual Meeting, New Orleans, USA, 1173-1177.

Johnson, D.H., 2013. Practical application of time-lapse seismic data. SEG Distinguished Instructor Series, No. 16.

Kennett, B.L.N., 1983. Seismic wave propagation in stratified media. Cambridge University Press, ISBN: 3-7643-6677-X.

Landrø, M., 2001. Discrimination between pressure and fluid saturation change from time-lapse seismic data. Geophysics 66, 836-844.

Liu, E., Martinez, A., 2012. Seismic fracture characterization: Concepts and practical applications. EAGE Publications, ISBN: 9073834503-9789073834507.

MacBeth, C., Shams, A., 2006. Observation of azimuthal anisotropy from the seismic reflectivity of a Tertiary turbidite sand. Geophysical Prospecting 54(5), 553-564.

Mattocks, B., Todorovic-Marinic, D., Li, J., Roche, S.L., Ronen, S., 2005. PS-wave and P-wave azimuthal anisotropy in a carbonate basin. EAGE/SEG Research Workshop, Pau, France, A30.

Molotkov, L.A., Červený, V., Novotný, O., 1976. Low-frequency and high-frequency expressions for the reflection and transmission coefficients of seismic waves for transition layers. Studia Geophysica et Geodaetica 20, 219-235.

Olofsson, B., Probert, T., Kommedal, J.H., Barkved, O.I., 2003. Azimuthal anisotropy from the Valhall 4C 3D survey. The Leading Edge 22, 1228-1235.

Ramos, A.C.B., Castagna, J.P., 2001. Useful approximations for converted-wave AVO. Geophysics 66, 1721-1734.

Rüger, A., 1997. P-wave reflection coefficient for transversely isotropic models with vertical and horizontal axis of symmetry. Geophysics 62, 713-722.

Rüger, A., 1998. Variation of P-wave reflectivity with offset and azimuth in anisotropic media. Geophysics 63, 935-947.

Sayers, C.M., 2010. Geophysics under stress: Geomechanics applications of seismic and borehole acoustic waves. EAGE Publications, ISBN: 1560802103-9781560802105.

Segura, J.M., Fisher, Q.J., Crook, A.J.L., Dutko, M., Yu, J.G., Skachkov, S., Angus, D.A., Verdon, J.P., Kendall, J-M., 2011. Reservoir stress path characterization and its implications for fluid-flow production simulations. Petroleum Geoscience 17, 335-344.

Shams, A., MacBeth, C., 2003. Detection of saturation changes in a turbidite sand by 4D AVOA. EAGE 65th Conference & Exhibition, Tunis, Tunisia, A-31.

Stovas, A., Landrø, M., 2005. Fluid-pressure discrimination in anisotropic reservoir rocks – A sensitivity study. Geophysics 70, O1-O11.

Thomsen, L., 1986. Weak elastic anisotropy. Geophysics 51, 1954-1966.

Tsvankin, I., 1997. Reflection moveout and parameter estimation for horizontal transverse isotropy. Geophysics 62, 614-629.

Verdon, J.P., Angus, D.A., Kendall, J-M., Hall, S.A., 2008. The effect of microstructure and nonlinear stress on anisotropic seismic velocities. Geophysics 73, D41-D51.

Wang, S.X., Li, X.Y., DI, B.R., Booth, D., 2010. Reservoir fluid substitution effects on seismic profile

interpretation: A physical modeling experiment. Geophysical Research Letters 37, L10306.
Yuan, S.Y., Wang, S.X., Sun, W.J., Miao, L.N., Li, Z.H., 2014. Perfectly matched layer on curvilinear g rid for the second-order seismic acoustic wave equation. Exploration Geophysics 45, 94-104.
Zheng, Y., 2006. Seismic azimuthal anisotropy and fracture analysis from PP reflection data. Ph.D. thesis, University of Calgary.

Appendix A. Dynamic elastic model construction from the output of integrated hydro-mechanical simulations

For the two-fault graben-style reservoir model having high and low fault fluid-flow transmissibility, the integrated reservoir fluid-flow and geomechanical simulations were implemented through explicitly coupling (two-way iteratively or loosely) the TEMPEST reservoir simulation model (Roxar Ltd.) for the fluid-flow calculations within the producing reservoir and the finite element based ELFEN simulator (Rockfield Ltd.) for the geomechancial deformation predictions and stress path evolutions within the reservoir and the bounding rocks. An MPI interface is used to pass pore pressure calculations from TEMPEST to ELFEN and pore volume changes from ELFEN to update TEMPEST (Angus et al. 2011; Segura et al. 2011). Geomechanical deformation is dependent on the Young's modulus (E) and Poisson's ratio (υ), as well as the porosity (ϕ). The assumed Young's modulus and Poisson's ratio are: $E = 5.35\phi^{-0.372}$ GPa and $\upsilon = 0.45$ for the bounding material, and $E = 13.8\phi^{-0.4}$ GPa and $\upsilon = 0.25$ for the non-sandstone reservoir (Segura et al. 2011).

The effective stress tensor, pore-fluid pressure and static stiffness (high strain magnitude, low strain rate) are output every six month of the coupled simulation and are used as input for the micro-crack rock physics model (Verdon et al. 2008; Angus et al. 2009) to construct the dynamic elastic models (dynamic stiffness) for seismic response prediction (see Figure A.1). An initial crack density η^0 and an initial aspect ratio a^0 are used for the micro-crack rock physics model and have been calibrated using dry and saturated core data from the literatures. For the graben reservoir model, the values used are: $\eta^0 = 0.25$ and $a^0 = 0.001$ for the sandstone reservoir and $\eta^0 = 0.125$ and $a^0 = 0.0005$ for the non-reservoir shale (Angus et al. 2009). The stress-dependent rock physics

model creates the 21 components of the full dynamic stiffness tensor, to describe the full seismic response for wave propagation through anisotropic media.

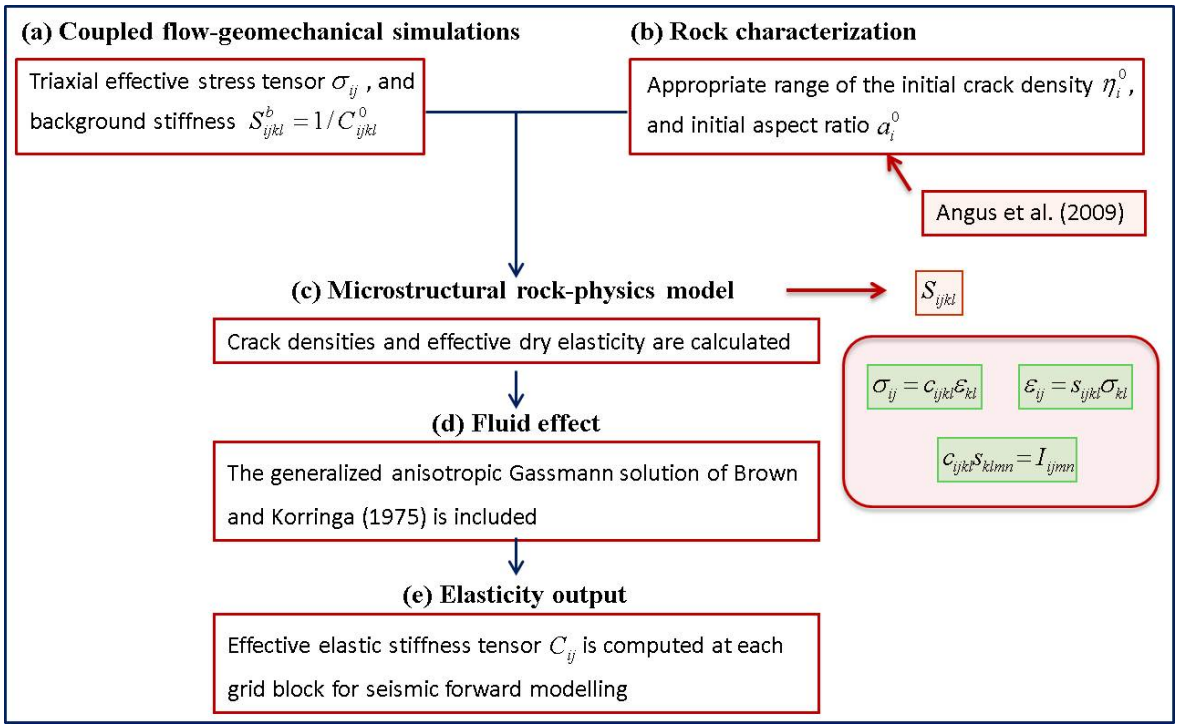

Figure A.1. Workflow to construct stress-dependent dynamic elastic model based on the output of coupled fluid-flow and geomechanical simulations using the analytical microcrack nonlinear stress elasticity dependency rock-physics model. Figure from Verdon et al. (2008) and Angus et al. (2009) with some modifications.